



Particle temperature effect in cold spray: A study of soft particle deposition on hard substrate

A. Nastic^{a,*}, B. Jodoin^a, D. Poirier^b, J.-G. Legoux^b

^a University of Ottawa Cold Spray Laboratory, Ottawa, ON, Canada

^b National Research Council of Canada, Boucherville, QC, Canada



ARTICLE INFO

Keywords:

Particle temperature influence
Upstream/downstream injection
Numerical critical velocity
Coating adhesion
Pseudo-plasticity
In-situ peening

ABSTRACT

In cold spray, the interactions between feedstock particles and propellant gas control deposition outcome. The particle impact temperature, along with impact velocity, governs the deposition due to its effect on the impact deformation processes. As bonding mechanisms rely primarily on the particle/substrate plastic flow upon impact, particle impact temperature holds a predominant role in process optimization.

The current work studies the effect of pure aluminum particle impact temperature on deposition phenomena when propelled onto a hard steel substrate. Particle impact temperature was varied while achieving the same particle impact velocity, using low and high-pressure cold spray systems. Three different particle diameters are studied, with varying resulting inherent impact temperatures, to provide size dependent insight on deposition/adhesion.

Experimental results demonstrate that at low particle impact temperature, i.e. 50 °C, coating adhesion is controlled by in-situ peening. Adhesion shifts to particle in-flight characteristics dependent bonding, i.e. $\eta = V/V_c$, as particle temperature increases. At low particle impact temperatures, the coating bond strength increases with increasing in-situ impingement intensity and frequency, i.e. decreasing deposition efficiency with increasing particle size. At higher particle impact temperatures, in-situ peening rate decreases and the adhesion strength increases with decreasing particle size. In addition to affecting the impact process (DE, V_c and adhesion), the particle impact temperature also influences the coating mechanical properties through the creation of temperature-dependent crack propagation mechanisms, i.e. deflection, bridging and acceleration, and of particle-particle structural arrangement related to deformation processes, i.e. fish scale effect and pseudo-plasticity behavior.

1. Introduction

The cold gas dynamic spray (CGDS) process, or simply cold spray (CS), is used for the deposition of various materials and has become a promising method in multiple material processing fields, including additive manufacturing [1–3]. CGDS is based on the energy exchange between a gas flow and injected powder material. The gas stream (nitrogen, helium or air) is directed through a converging/diverging nozzle to reach the supersonic regime. Particles are injected into the nozzle and propelled to high velocities reaching values between 300 m/s and 1200 m/s [4,5]. Upon impact with a target surface (substrate), up to 90% of the particle kinetic energy is converted into heat, while the remaining energy is used for viscoelastic and elastic deformations of particle and substrate. The successful adhesion of the impacting material depends on

various phenomena that initiate due to the high strain rate plastic deformation occurring at the impact boundaries [5–8]. Reported strain and strain rates at the particle/substrate interface reach values of 10 and 10^9 s⁻¹, respectively [9], which are far beyond values commonly encountered in classical powder manufacturing methods [10,11]. These extreme material deformation phenomena lead to surface oxide layer breakup, localized melting, amorphization, diffusion, shear instability and hydrodynamic plasticity [8,12,13], which have all been associated to bonding processes.

Aside from the particle material properties, the CGDS impact dynamics rely on in-flight particle/gas momentum and energy exchange processes. The process gas stagnation pressure and temperature govern the flow dynamics and thus particle in-flight characteristics [14–16]. The particle/gas mixture undergoes large changes in many properties inside and outside the nozzle. Furthermore, the occurrence of oblique

* Corresponding author.

E-mail address: aleksandra.nastic@uottawa.ca (A. Nastic).

List of symbols	
<i>P</i>	flow pressure (N/m^2)
<i>V</i>	flow velocity (m/s)
<i>T</i>	flow temperature (K)
<i>u_i</i>	gas velocity component in <i>i</i> -direction (<i>i</i> = 1, 2, 3) (m/s)
<i>ρ</i>	density (kg/m^3)
<i>C_D</i>	drag coefficient (-)
<i>t</i>	time (s)
<i>k</i>	turbulent kinetic energy (m^2/s^2)
<i>ε</i>	turbulent dissipation rate (m^2/s^3)
<i>μ</i>	viscosity ($\text{kg}/\text{m s}$)
<i>α_ε</i>	inverse effective Prandtl number for turbulent dissipation rate (-)
<i>Pr_t</i>	turbulent Prandtl number (-)
<i>S_M</i>	particle phase influence on gas momentum ($\text{kg}/\text{m}^2 \text{ s}^2$)
<i>Y_M</i>	contribution of the fluctuating dilatation in compressible turbulence to dissipation rate ($\text{kg}/\text{m s}^3$)
<i>G_k</i>	generation of turbulence kinetic energy due to mean velocity gradient ($\text{kg}/\text{m s}^3$)
<i>G_b</i>	generation of turbulence kinetic energy due to buoyancy ($\text{kg}/\text{m s}^3$)
<i>C_{1, 2, 3c}</i>	RNG <i>k</i> - <i>ε</i> turbulent model constants (-)
<i>h_{tot}</i>	total system enthalpy ($\text{kg m}^2/\text{s}^2$)
<i>n</i>	normal direction coordinate (-)
<i>k₁</i>	particle-size-dependent fitting parameter (-)
<i>x_i</i>	Cartesian coordinate in the <i>i</i> -direction (<i>i</i> = 1, 2, 3) (m)
<i>n_s</i>	spread factor (-)
<i>Re_p</i>	particle Reynolds number (-)
<i>L_p</i>	average distance between particles (m)
<i>L</i>	characteristic length (m)
<i>Z</i>	mass ratio, powder/gas (-)
<i>d</i>	particle diameter (m)
<i>Volume</i>	volume flow rate (m^3/s)
<i>m̄</i>	mass flow rate (kg/s)
<i>ρ̄</i>	density flow rate ($\text{kg}/\text{m}^3 \text{ s}$)
<i>F_b</i>	body force ($\text{kg m}/\text{s}^2$)
<i>A</i>	cross-sectional area (m^2)
<i>D</i>	level of particle interactions (-)
<i>Π_{mom}</i>	momentum coupling ($\text{kg m}^2/\text{s}^2$)
<i>λ</i>	thermal conductivity ($\text{kg m}/\text{s}^3 \text{ K}$)
<i>a_k</i>	inverse effective Prandtl number for turbulent kinetic energy (-)
<i>τ</i>	stress tensor in viscous dissipation term ($\text{kg}/\text{m s}^2$)
<i>S_k, S_ε</i>	user-defined source terms ($\text{kg}/\text{m s}^3$)
<i>C_v</i>	specific heat at constant volume ($\text{m}^2/\text{s}^2 \text{ K}$)
<i>β, η₀</i>	RNG constants (-)
<i>S</i>	modulus of the mean rate-of-strain tensor (1/s)
<i>σ</i>	particle material tensile strength (N/m^2)
<i>Y_d</i>	cumulative percentage (%)
<i>Nū</i>	average Nusselt number (-)
<i>M_p</i>	particle Mach number (-)
Abbreviations	
<i>BSD</i>	backscattered detector
<i>CFD</i>	computational fluid dynamics
<i>CGDS</i>	cold gas dynamic spray
<i>CS</i>	cold spray
<i>CSM</i>	cold spray meter
<i>DE</i>	deposition efficiency
<i>DRW</i>	discrete random walk
<i>FEM</i>	finite element model
<i>HPCS</i>	high pressure cold spray
<i>HPIT</i>	high particle impact temperature
<i>LPCS</i>	low pressure cold spray
<i>LPIT</i>	low particle impact temperature
<i>PBI</i>	polybenzimidazole
<i>RANS</i>	Reynolds Averaged Navier-Stokes
<i>RNG</i>	re-normalized group
<i>SEM</i>	scanning electron microscopy
<i>V_c</i>	critical velocity
<i>R_a</i>	arithmetic surface roughness
Subscripts	
<i>eff</i>	effective
<i>g</i>	gas
<i>i</i>	<i>i</i> th coordinate variable (=1, 2, 3 vector component)
<i>j</i>	Einstein summation of <i>j</i> = 1, 2, 3
<i>m</i>	melting
<i>p</i>	particle
<i>t</i>	turbulent

shocks and Mach disks, inducing abrupt discontinuity and instantaneous variation in gas flow characteristics can significantly affect the particle thermal history prior to impact [17,18]. A few studies have captured the gas stream phenomenological characteristics using Schlieren photography [19,20]. Computational fluid dynamics (CFD) models have also been used to study the driving gas behavior with the objective of assessing the particle impact velocity and temperature. These CFD efforts have generated physically realistic flow simulations [17,18,21,22]. CGDS particle velocities have been measured through laser-light sheet, laser two focus velocimetry and high speed cameras [23–31]. These experimental observations have been used to develop proper momentum transfer models, contributing to adequate prediction of the particle impact velocity influence on deformation and deposition [32–36]. However, the low particle temperatures in the CGDS process coupled with high particle velocities prohibit the use of classical optical pyrometry, which makes any CGDS particle temperature measurement a technical challenge. In a recent study, CGDS particle in-flight temperature measurements have been successfully reported [14], allowing the evaluation and development of a proper particle transient heat transfer model. Many have reported various benefits of increasing particle impact temperature on deposition and adhesion, which have been

related to improved particle deformation promoting the creation of zones suitable for bonding [37–39]. To support this assertion, use of external powder preheating systems has shown to increase DE and adhesion in low-pressure CS systems using downstream injection [39–42]. Analogously, in high-pressure CS systems, in which the powder injection is made axially in the converging section, reported DE's reach up to 95% (Cu on Al) [33,43] as heat transfer processes are promoted in the stagnant pre-chamber high temperature gas.

Therefore, the primary objective of the current work is to investigate the effect of particle impact temperature and size on deposition for soft particle/hard substrate material combination. The influence of particle impact temperature on deposition characteristics (deposition efficiency and critical velocity), adhesion and coating properties (apparent ductility) are studied. Low and high-pressure cold spray systems (LPCS and HPCS) have been utilized to generate deposits with similar particle impact velocities but different particle impact temperatures. Since particle impact temperature measurement is impossible at the chosen working parameters, validated CFD model correlations are applied to obtain particle impact temperature values [14]. Particle velocities are measured and used to additionally validate the developed CFD model's accuracy. The particle injection location and particle trajectory are used

to explain the statistical particle in-flight characteristics. The experiments are conducted for three distinct particle size ranges to provide a size-dependent analysis.

2. Experimental procedures

2.1. Feedstock powder

Spherical commercially pure aluminum feedstock powder has been used (Equispheres, ON, CA) in the generated deposits. Three distinct sets of powders with different size diameter distributions have been selected to study the effect of particle size on impact temperature and its influence on coating deposition and bonding developments. Fig. 1a presents the particle size distribution for all three powder sets. The powder sets are referred to as set 1, set 2 and set 3 and present an average powder size of 40 µm, 58 µm and 68 µm respectively. As shown in Fig. 1b, c and d, using electron microscopy (SEM, Zeiss, EVO-MA10, UK) images under the detection of backscattered electron detector (BSD), all three powder sets exhibit a spherical shape with negligible presence of satellites.

2.2. Substrate material

A common low carbon steel material, SAE1018 (25.4 mm diameter and 40 mm height) with measured hardness of 90.5 ± 0.3 HRB has been used as substrate, which ensures a proper study of soft material impact on hard target surface. Surface preparation and coating depositions were performed on the flat ends of the cylindrical samples. Two surface preparation methods have been utilized. A mirror finish surface has been obtained by gradual grinding and polishing steps up to a final process using 3 µm abrasive suspensions. A grit blasting method using a 20mesh (850 µm) ferrosilicate abrasive was also utilized as a second surface preparation method to roughen the substrate surface. Prior to the deposition process, all substrates have been cleaned and degreased using ethanol. During coating deposition, all substrates have been thermally insulated from the surroundings to avoid uncontrolled substrate temperature variations. A portable profilometer (PHASE II SRG-4000A, NJ, USA) equipped with a diamond stylus has been used to obtain the

arithmetic surface roughness, R_{a} , of polished substrates. A digital optical microscope (VHX-2000 Keyence Corporation, Osaka, Japan) has been utilized, on the other hand, to obtain profile depths of grit blasted samples, which have been subsequently imported in Matlab for the calculation of surface R_{a} [44].

2.3. Cold spray depositions

Commercially available CS systems (SST-EP, CenterLine Limited, Windsor, ON, CA and Oerlikon Metco KINETIKS 4000, Schwytz, CH) have been utilized to deposit the aluminum powders. In the SST-EP system, the powder is injected radially in the diverging nozzle section. A PBI nozzle has been used for all deposition made with the LPCS [45]. Due to the significant particle trajectory deviation shown to occur after particle nozzle wall deterioration from impact wear [45], a new unworn PBI nozzle has been utilized for all deposits. The powder injection in the HPCS system is located in the center of the converging nozzle section, parallel to the nozzle axis. A SiC nozzle has been used in the KINETIKS 4000 system. The nozzles geometries and dimensions are presented in detail in Section 3.1. Table 1 presents the spray parameters used when operating each system, which ensured comparable particle impact velocities while providing different particle impact temperatures.

Powder feeding rate was kept similar for all sprays (≈ 20 g/min). Deposition efficiency (DE) has been measured using the specimen weight gain with respect to the total powder weight propelled at the

Table 1
CGDS process deposition parameters and features.

	SST-EP	KINETIKS 4000
Powder injection location	Downstream	Downstream
Nozzle material	Polymer	SiC
Stagnation temperature	500 °C	500 °C
Stagnation pressure	3.4 MPa	3.4 MPa
Traverse velocity	10 mm/s	150 mm/s
Number of passes	1	15
Stand-off distance (SOD)	15 mm	15 mm
Step size	1 mm/pass	1 mm/pass

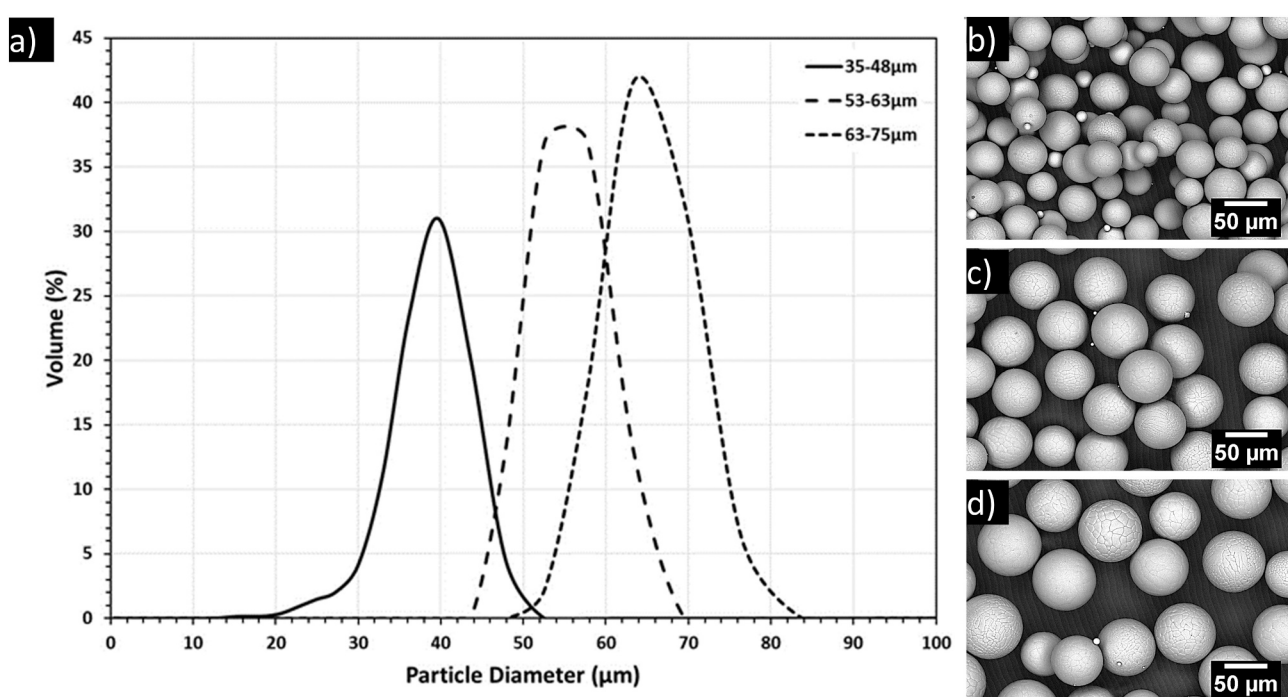


Fig. 1. a) Feedstock powder size distribution. The geometry and size of all three powder sets are depicted in b) set 1, c) set 2 and d) set 3 using backscattered scanning electron microscope (BSD-SEM) images.

substrate surface. As presented in Table 1, the LPCS deposits have been made using two gun traverse velocities, i.e. 10 mm/s and 150 mm/s, while only 150 mm/s was utilized for HPCS deposits due to the robot minimum speed limit. For the LPCS, spot sprays, i.e. powder deposition at a single gun position, have also been carried out to characterize the particle spatial position upon deposition. Obtained coating microstructural analysis has been performed through digital optical microscopy and scanning electron microscopy using secondary (SE) and back-scattered detectors.

2.4. Particle velocity measurement

The in-flight particle velocity was measured at a distance of 15 mm from the nozzle exit using a Cold Spray Meter (CSM) eEvolution (Tecnar Automation Ltd., St-Bruno, Canada). The CSM is equipped with a continuous 810 nm wavelength laser that illuminates particles as they cross a dual-slit photomask. The diffracted light is subsequently captured and collected data filtered by an internal interpreting system. The velocity is calculated using the traveling distance and time interval that the detected particle takes to cross two mask slits. For statistical purposes, a minimum of 1000 individual particle velocities have been measured for each conducted tests. The velocity readings have been made at the center of the nozzle for all cases.

2.5. Adhesion tests

Coating adhesion strength values have been obtained and evaluated following the ASTM-C633 standard [46]. A thermally curing elastomeric adhesive, FM-1000 (Cytec Engineering Materials, MD, USA) has been used to glue the cylindrical coated substrates to counter uncoated steel cylindrical specimens. Prior to testing, all coatings have been machined to a 550 μm thickness. Once cured and cooled to room temperature, the assembly has been pulled using a universal tensile testing machine (Instron Series 4482, MA, US) at a rate of 0.017 mm/s and failed coating fracture surfaces have been subsequently analyzed. Three to five

coatings have been tested per spray set.

2.6. Bend-to-break tests

Bend-to-break tests have been performed, following a procedure similar to the ASTM D4145-10 standard [47], using coatings deposited on grit blasted surfaces. After machining the coatings down to 550 μm thickness, natural interfacial delamination occurring during high speed saw cutting processes allowed proper coating removal from the steel substrate. The machined surface was placed under tension while the other side (initially bonded to the roughened substrate surface) was put under compression to avoid pre-mature crack propagation and arbitrary surface roughness dependant results.

3. Computational fluid dynamics

3.1. Geometry and operating conditions

The commercially available Computational Fluid Dynamics (CFD) ANSYS Fluent 19 software was used to model the carrier and driving gas flows and particulate phase for both spray systems. The three-dimensional meshing systems, comprised of approximately 2 million cells, are shown in Fig. 2. The meshing process was generated through ANSYS WB Meshing Tool by discretizing the computational domain into separate grids and using edge sizing with a biased growth rate to increase resolution near the nozzle walls. A grid dependency study was performed to determine the appropriate grid size ensuring grid independency. The substrate surface, modeled as an adiabatic wall, was placed at the end of the atmospheric environment at the corresponding 15 mm stand-off distance. The surrounding environment was set at a radius of 80 mm to avoid disturbance on the flow field. The solutions were considered converged when the residuals were decreased by at least three orders of magnitude. In addition, the mass imbalance was also verified ($\sim 8\text{e}^{-8} \text{ kg/s}$) at convergence.

Pressure-based boundary conditions were applied at the main gas

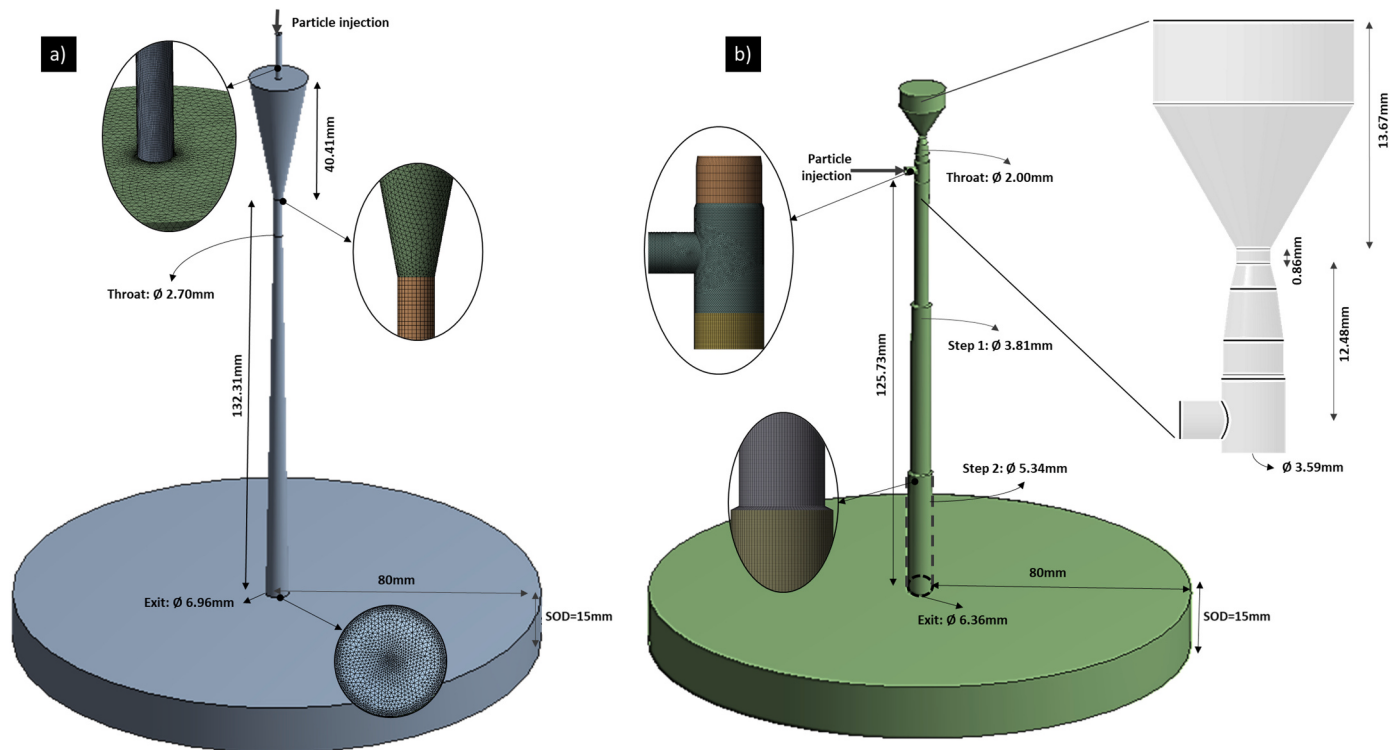


Fig. 2. Three-dimensional computational domain dimensions and meshing details for both CGDS systems. a) Upstream powder injection (HPCS system) and b) downstream powder injection (LPCS system).

inlet and outlet of each nozzle and the flow was treated as a compressible flow. Mass flow rate boundary conditions, based on used experimental set-up, were set to 0.00033 kg/s and 0.0036 kg/s for the powder feeding line nitrogen flow in the LPCS and HPCS cases respectively. A no-slip condition was enforced on all nozzle walls. The various boundary conditions are summarized in Table 2.

3.2. Gas flow model

The Reynolds Averaged Navier-Stokes (RANS) equations along with the re-normalized group (RNG $k-\epsilon$) turbulence model were utilized to model the gas flow structure inside and outside the converging/diverging nozzle. The RANS-based model accounts for the effect of turbulence while greatly reducing the required computational resources. A total of six governing equations have thus been utilized: conservation of mass and energy, momentum balance (in three dimensions) and turbulent kinetic energy. The continuity equation is written as follow;

$$\frac{\partial \rho}{\partial t} + \frac{\partial}{\partial x_i} (\rho u_i) = 0, \quad (1)$$

where ρ is the gas flow density, t is the time, u_i is the flow velocity in the i direction and x_i is a coordinate variable in space. The momentum balance is provided by;

$$\frac{\partial}{\partial t} (\rho u_i) + \frac{\partial}{\partial x_j} (\rho u_i u_j) = \frac{\partial}{\partial x_j} \left[-P + \mu_{eff} \left(\frac{\partial u_i}{\partial x_j} + \frac{\partial u_j}{\partial x_i} \right) \right] + S_M, \quad (2)$$

where P is the pressure, which includes an additional term due to the turbulent normal stress, S_M represents the mass added to the gas phase from the dispersed particulate phase or the momentum change it generates to the gas phase in each coordinate system and μ_{eff} accounts for turbulent viscosity as follow;

$$\mu_t = \rho C_\mu \frac{k^2}{\epsilon}, \quad (3)$$

where $C_\mu = 0.0845$ [48]. The k and ϵ terms are obtained using the following respective differential transport equations;

$$\frac{\partial}{\partial t} (\rho k) + \frac{\partial}{\partial x_i} (\rho k u_i) = \frac{\partial}{\partial x_j} \left[\mu_{eff} \alpha_k \left(\frac{\partial k}{\partial x_j} \right) \right] + G_k + G_b - Y_M + S_k - \rho \epsilon, \quad (4)$$

and

$$\frac{\partial}{\partial t} (\rho \epsilon) + \frac{\partial}{\partial x_i} (\rho \epsilon u_i) = \frac{\partial}{\partial x_j} \left[\mu_{eff} \alpha_\epsilon \left(\frac{\partial \epsilon}{\partial x_j} \right) \right] + C_{1\epsilon} \frac{\epsilon}{k} (G_k + C_{3\epsilon} G_b) - C_{2\epsilon} \rho \frac{\epsilon^2}{k} + S_\epsilon - R_\epsilon, \quad (5)$$

where $C_{1\epsilon}$, $C_{2\epsilon}$ and $C_{3\epsilon}$ are turbulent constants depending on the application and simulation conditions [49]. The α_ϵ and α_k quantities are the inverse effective Prandtl numbers for k and ϵ terms, respectively. G_k and G_b represent the generation of turbulent kinetic energy due to the mean

Table 2
Numerical model boundary conditions.

Location	P	V	T
Nozzle inlet	Specified stagnation	$\frac{\partial V}{\partial n} = 0$	Specified stagnation
Powder inlet	N/A (mas flow rate specified)	$\frac{\partial V}{\partial n} = 0$	Room temperature
Surrounding atmosphere	Ambient condition	$\frac{\partial V}{\partial n} = 0$	$\frac{\partial T}{\partial n} = 0$
Substrate/nozzle walls	$\frac{\partial P}{\partial n} = 0$	0	$\frac{\partial T}{\partial n} = 0$

velocity gradients and due to the buoyancy, respectively, while the S_k and S_ϵ are user-defined source terms. The RNG additional term, R_ϵ , in the dissipation rate equation is given by;

$$R_\epsilon = \frac{C_\mu \rho \eta^3 (1 - \eta/\eta_0)}{1 + \beta \eta^3} \frac{\epsilon^2}{k}, \quad (6)$$

where $\eta \equiv Sk/\epsilon$ and in which S refers to the modulus of the mean rate-of-strain tensor, $\eta_0 = 4.33$ and $\beta = 0.012$ [48].

The model total energy or total enthalpy (h_{tot}) modified for the Reynolds average energy equation is given by;

$$\frac{\partial}{\partial t} (\rho h_{tot}) - \frac{\partial}{\partial t} + \frac{\partial}{\partial x_j} (\rho u_j h_{tot}) = \frac{\partial}{\partial x_j} \left(\lambda \frac{\partial T}{\partial x_j} + \frac{\mu_t}{Pr_t} \frac{\partial h}{\partial x_j} \right) + \frac{\partial}{\partial x_j} [u_i (\tau_{ij} - \rho \bar{u}_i \bar{u}_j)] + S_T, \quad (7)$$

where Pr_t is the turbulent Prandtl number, S_T is the source term expressing the heat transfer between the flow and particles, τ is the stress tensor and λ is the thermal conductivity. The total enthalpy refers to the total energy of the system including viscous work, such that;

$$h_{tot} = C_v T + \frac{1}{2} (u_i u_i) + k. \quad (8)$$

The additional terms, i.e. S_M and S_T , provided in Eqs. (2) and (7) respectively, have been neglected due to the high Stokes number, St , and low momentum coupling interactions parameter, Π_{mom} obtained in the current study. The momentum coupling expressed in the following equation, is used to assess the impact of the aluminum particle phase on the nitrogen gas flow;

$$\Pi_{mom} = \frac{Z}{\frac{\rho_p d^2 V}{18 \mu_g L} + 1}, \quad (9)$$

where the subscript p and g refer to the particle and gas phase respectively, d is the particle diameter, L is the characteristic length, i.e. diameter of the nozzle at a specific location, and Z is the mass ratio of powder to gas. The momentum coupling parameter has been calculated and is less than 5% in all cases, such that the gas phase momentum variation due to the presence of particles has not been included [50]. In addition, many have used the volumetric, *Volume*, particle to gas flow ratio to evaluate the significance of the particle phase influence on the gas flow [41,51,52];

$$\frac{Volume_p}{Volume_g} = \frac{\dot{m}_p}{\dot{m}_g} \cdot \frac{\dot{\rho}_g}{\dot{\rho}_p}, \quad (10)$$

where \dot{m} and $\dot{\rho}$ are the mass and density flow rate, respectively. Provided that $\rho_g \ll \rho_p$ holds and that the powder feed rate used in the current study is 20 g/min, a ratio less than 1% is obtained indicating negligible effects. Particle-particle interactions can also influence the behavior of the particulate flow. The particle level of interactions can be described using the mean distance between particles, L_p , to the average particle diameter, $d_{average}$:

$$D = \frac{L_p}{d_{average}}. \quad (11)$$

Since values over ten have been obtained in the current study, the particles are considered isolated and the particle to particle interactions have been neglected [52]. Based on the above discussion details and analysis, a one-way coupled Lagrangian particle tracking method has been assessed as appropriate [50,51,53,54]. A density-based solver with a Green-Gauss node-based gradient method was utilized to model the nitrogen gas stream features. The ideal gas law has been used to account for the compressibility effects and a two-coefficient temperature-dependant Sutherland law is used to express viscosity variations with temperature [14]. Table 3 provides a summary of the gas and particle characteristics utilized in the current computational work.

Table 3
Simulated phase properties included in the computational work.

	Nitrogen gas	Aluminum particles
Diameter	N/A	Set measured distribution
Stagnation parameters	500 °C, 3.45 MPa	N/A
Density	Ideal gas	2710 kg/m ³
Specific heat capacity	1040.67 J/kg K	910 J/kg K
Thermal conductivity	0.0242 W/m K	210 W/m K
Viscosity	Sutherland law	N/A
Initial velocity at carrier gas injection (LPCS, HPCS)*	(30 m/s, 33 m/s)	(30 m/s, 33 m/s)
Initial temperature at carrier gas injection (LPCS, HPCS)	(25 °C, 25 °C)	(25 °C, 25 °C)

* The particulate phase reaches the carrier gas flow velocity upon its injection into the driving gas flow.

3.3. Discrete phase/particle

3.3.1. Momentum and heat transfer

The particle phase was modeled as an inert point in space using a Lagrangian method. The velocity and trajectory of the discrete phase, i.e. the aluminum particles, in the two-phase model was computed using a drag force balance, i.e. Newton's balance equation.

$$m_p \frac{dV_p}{dt} = \frac{1}{2} C_D \rho A_p (V - V_p)^2 + F_b \quad (12)$$

where m_p , C_D , A_p and F_b are the particle mass, particle drag coefficient, particle cross-sectional area and additional body forces. The particle possible deceleration due to the adverse pressure gradient generated at the substrate surface bow shock is also taken into account and included in the F_b term. The body force per unit mass is given as;

$$F_b = \left(\frac{\rho}{\rho_p} \right) V_p \cdot \nabla V \quad (13)$$

No other additional body forces have been added to the equation as the common gravity, lift, thermophoretic and electrostatic forces provide little influence on the particle momentum in the CGDS process.

The Henderson drag correlations, for C_D term definition, have been used to describe the particle momentum [55]. According to previous studies, the Henderson correlation, which covers a wide range of particle Mach and Reynolds numbers and describes flow motion from incompressible to free molecular regimes, has shown accurate results based on experimental particle-laden flow measurements [14,15,56–60]. The transient particle heat transfer processes are calculated assuming a lumped capacitance method and the energy balance equation from the first law of thermodynamics is used [14,23,61]. Details describing the terms involved in the analysis can be found in a previous study [14]. The following Nusselt, \bar{Nu} , correlation has been utilized to define the average convective heat transfer coefficient;

$$\bar{Nu} = 2 + 0.44 Re_p^{0.5} Pr^{0.33} \exp(0.1 + 0.872 M_p), \quad (14)$$

which is valid for particle Mach numbers above 0.24. In all other cases the common Ranz-Marshall model is utilized [62]. The correlation described in Eq. (14) has been shown to provide accurate particle temperature readings based on recent CGDS experimental work [14].

3.3.2. Stochastic trajectory

Since the flow is turbulent, a stochastic tracking approach, referred to as the discrete random walk (DRW) model, is applied to simulate the particle turbulent dispersion ensuring representative particle trajectories. Numerous studies conducted in the CGDS field have shown that the DRW does provide an accurate particle dispersion [41,51,54,63]. DRW computes the trajectory of each particle based on the statistical

sum of the mean and turbulent velocity component of the gas. In addition to the statistical velocity measurement, an integral time scale is utilized, which accounts for the rate of turbulent kinetic energy dissipation. This time scale is linked to the characteristic lifetime of an eddy. It is assumed that a particle is in contact with the turbulent eddy for whichever time is shorter between the eddy lifetime and eddy crossing time. Sufficiently large numbers of DRW runs have been used to ensure that trajectories include the statistical effect of turbulent dispersion.

3.3.3. Numerical size distribution

To model the particle size distribution for each powder set, the Rosin-Rammler distribution function has been utilized to generate proper particle size bins in ANSYS Fluent using;

$$Y_d = e^{-(d/\bar{d})^{ns}}, \quad (15)$$

where Y_d represents the cumulative percent retained at size d and \bar{d} and n_s are fitting parameters, referred to as the average diameter and spread factor. The obtained spread factor is 4.07, 13.87 and 14.33 for set 1, set 2 and set 3 respectively. Following the injection of accurate particle diameter bins, a function generating a random selection of particles in each bin size has been included to obtain the actual measured distribution.

3.3.4. Particle/nozzle wall interactions

In the HPCS, the powder injection line is estimated to be perfectly aligned with the nozzle axis. As the feeder tube size is the same as the nozzle throat, the particle radial acceleration and movement is limited and particle-nozzle interactions are expected to be low [52]. The particle collisions are estimated to be perfectly elastic and as the particle-nozzle impact collisions are anticipated to be limited such estimation would have little effect on results if inaccurate. For the LPCS, however, significant particle/wall interactions are expected to occur due to the radial injection process. Experimental evaluation of the coefficient of restitution for impacts between metal particles and PBI material are not found in the literature. Wu et al. have investigated the rebound behavior of spheres traveling at 5 m/s during elastic-plastic oblique impacts using FEM [64]. Although the velocity is far below the particle velocities reached in the CGDS process, particles are expected to travel with much higher axial velocity than radial velocity due to the strong axial gas flow momentum. Based on their study, the tangential and normal coefficient of restitution are both chosen to be 0.8 in the current simulation work [52,64].

4. CFD results

The current section covers the CFD results used to assess the particle in-flight temperature, which cannot be measured [14]. The heat transfer analysis and correlations used have been validated elsewhere [14]. In addition, the accuracy and validity of the models for the current study have been evaluated using particle velocity measurements and single spot deposit. The CFD results are also used to visualize the flow structure and particle trajectory.

4.1. Gas flow properties

Fig. 3 shows the gas velocity contour maps of both spray systems up to the substrate surface. The gas velocity along the HPCS nozzle varies gradually and reaches about 1000 m/s at the nozzle exit, with a thin boundary layer all along the nozzle length. Cross-sectional inserts reveal that the carrier gas affects the driving gas, producing a slower core at the nozzle center, although mixing seems to minimize the effects towards the nozzle exit. In comparison, the gas velocity reaches high values much earlier in the LPCS system, with similar exit velocity. The expansion of the gas at each sharp step of the LPCS nozzle generates the formation of an expansion wave/oblique shock wave system, creating an

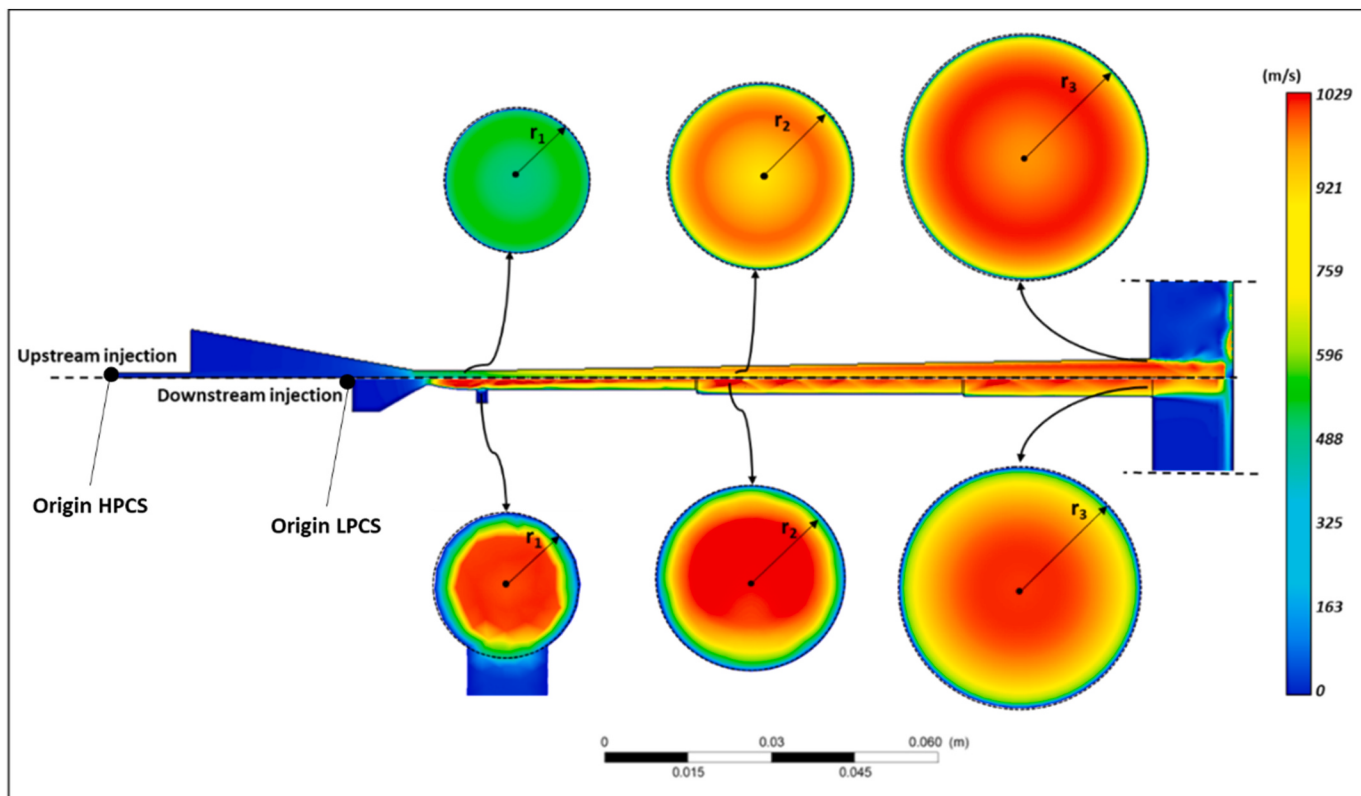


Fig. 3. 2D axial cross-sectional view of the gas flow velocity contour across the nozzle and exit region in the HPCS (top) and LPCS (bottom) systems. The gas velocity across the nozzle diameter at three selected regions (r_1 , r_2 and r_3) is shown in provided inserts.

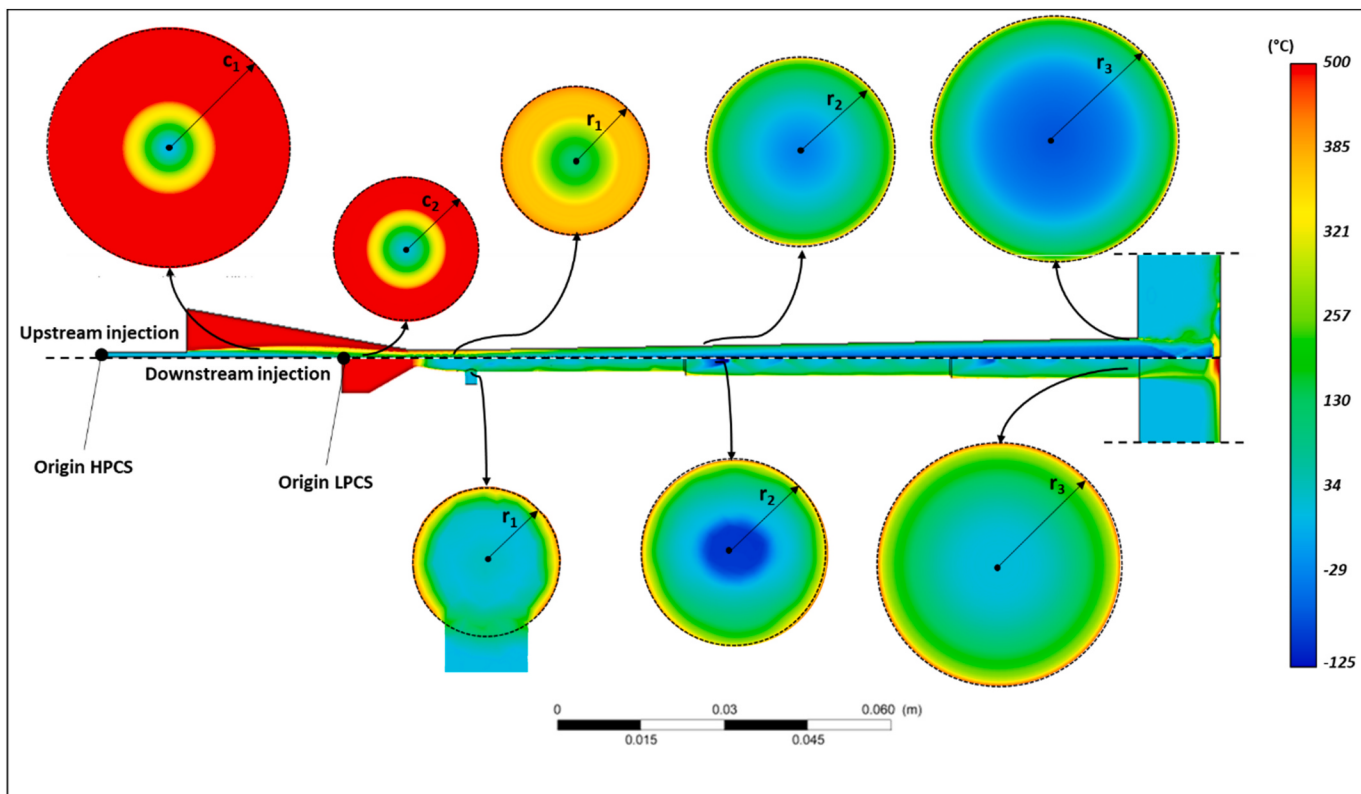


Fig. 4. 2D axial cross-sectional view of the nitrogen flow temperature contour across the nozzle and atmospheric regions in high (top) and low (bottom) pressure CS systems are provided. In the HPCS, the gas temperature in the converging section is illustrated using two cross-sectional inserts (c_1 and c_2). The gas temperature across the nozzle diameter at three regions in the diverging section (r_1 , r_2 and r_3) is shown using provided inserts for both systems.

oscillatory pattern in the gas flow that maintains/replenishes a high gas velocity outside the boundary layer zone. These structures stabilize after multiple reflections due to viscous effects, homogenizing the flow profile. Furthermore, the radial carrier gas injection also affects the driving gas properties. This main flow disturbance remains following the wall boundary layer, such that the high shock trail flow appears as a dis-symmetrical phenomenon. The carrier gas effect is damped after the first nozzle step.

The gas static temperature contour maps are shown in Fig. 4. In the HPCS nozzle, the gas temperature decreases gradually to reach around -75°C in the core, at the nozzle exit, as thermal energy is converted into kinetic energy. The cold carrier gas is clearly visible in r_1 and r_2 regions, which generates a colder central flow surrounded by the high temperature main flow. This cold core also limits the stagnation temperature in the converging section, i.e. regions c_1 and c_2 . In the LPCS nozzle, the oscillatory shock wave system generates local zones of very low temperature in the diverging nozzle section (-125°C in r_2). The gas core exits at around 50°C , due to the low nozzle expansion ratio and with an almost uniform thermal energy distribution.

Fig. 5 shows the gas temperature and velocity maps near the substrate surface for both CS systems. A normal bow shock occurs as a result of the flow adjustment to the downstream stagnation perturbation (substrate). An outward radial deflection of the primary flow follows. While this flow is attached for the LPCS configuration, it is a recirculating flow in the HPCS system, as shown in Fig. 5b. This difference has been associated to the dissimilar Reynolds number (Re) that each flow reaches in both systems, i.e. increasing Re have been linked to the generation of downstream wall-jet recirculation [65]. The flow mechanisms controlling the wall jet features are mainly the jet-edge expansion and its reflexion from the sonic line and wall-jet boundaries [66]. One can observe that while the LPCS jet reaches a stagnation temperature of 500°C in the zone under the normal shock, the HPCS jet reaches a temperature of 327°C only. It is expected that these temperatures could have an effect on the substrate temperature during spraying [65,67].

4.2. Effect of particle injection and size on in-flight characteristics

Examination of LPCS particle streak lines (only one streak line is shown as an example) reveals that all powder sets come into contact with the nozzle wall in zone 2, prior to the first nozzle step. This location corresponds to the zone shown to experience important nozzle erosion [45], confirming the accuracy of the computed particle path lines. The powder rebound path is dependent on particle size with larger particles being able to recoil further towards the nozzle center and cross the shock wave trail on their path from the wall to the center due to their higher inertia. This is reflected through the particle distribution in the velocity/temperature maps presented in Fig. 6. In addition, smaller particles are seen to accelerate and decelerate faster in the stream center and shear layer respectively. Hence, set 1 particles reach velocities up to 680 m/s at the nozzle exit while powder set 3 reaches 620 m/s . Analogously,

smaller particles heat transfer rate is larger than that of larger particles due to their larger specific surface. Although the particle temperature is seen to slightly increase in the high temperature shear layer at the nozzle wall, with a larger increase for smaller particles, their limited time in the wall boundary combined with fast velocities and trajectory in the cold central supersonic gas stream only permits slight increase in temperature. At the nozzle exit, particles from set 1, set 2 and set 3 reach temperatures up to 72°C , 58°C and 41°C respectively.

Fig. 7 shows the particle characteristics and overall spread in the HPCS. The high symmetry footprint of particle dispersion is attributed to the injection alignment with the nozzle axis. From zone 1 to zone 2, the particle stream widens due to the presence of turbulence and low gas velocity in the gas mixing area. Smaller particle having less inertia contribute mostly to the radial dispersion. However, from zone 2 to zone 4, the presence of the narrow throat and higher gas central velocity confines the majority of particles in the nozzle center. At the nozzle exit stream center, particle set 1 reaches velocities up to 690 m/s while set 3 particles are accelerated up to 625 m/s . Smaller particles are heated to a higher temperature as their spread towards the nozzle wall is more pronounced in the converging gas mixing area in zone 2. Analogously, colder particles at the exit of the nozzle originate from a mixture of cold particles coming from the cold un-mixed converging-throat center and from radially dispersed particles traveling in the cold slow diverging flow. As a result, set 1, 2 and 3 feedstock powder particles reach a wide spread of in-flight temperatures with values reaching 327°C , 227°C and 202°C respectively, at the nozzle exit.

In addition, for the three powder size sets and for both utilized CGDS systems, it was found that the bow shock and the 15 mm particle flow distance from the nozzle exit do not drastically affect the particle in-flight characteristics.

5. Experimental results

5.1. Particle in-flight velocity

In order to validate the model predictions and ensure particle temperatures can be inferred adequately from the model, particle velocity measurements were conducted at the center of the gas stream, and at distance of 15 mm from the nozzle exit, using feedstock powder set 2. The measurements provided average particle velocities of 668 m/s and 660 m/s for the HPCS and LPCS systems respectively. In addition, the numerical average particle velocities obtained at the same location generated average velocities of 620 m/s and 600 m/s for the HPCS and LPCS system respectively. This agreement between experimental and numerical results provides some reliability of the simulations and its additional use in finding particle in-flight characteristics. Consequently, as both systems provided similar particle impact velocities, it is assumed that all results can be properly compared for each powder set between the two CS systems.

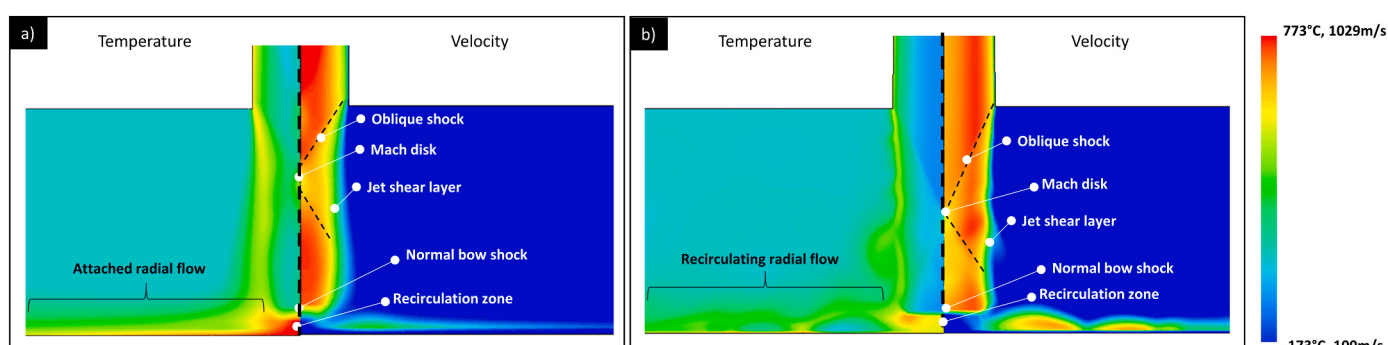


Fig. 5. Flow temperature and velocity at the substrate vicinity showing the radial gas flow regimes obtained in the a) LPCS and b) HPCS systems.

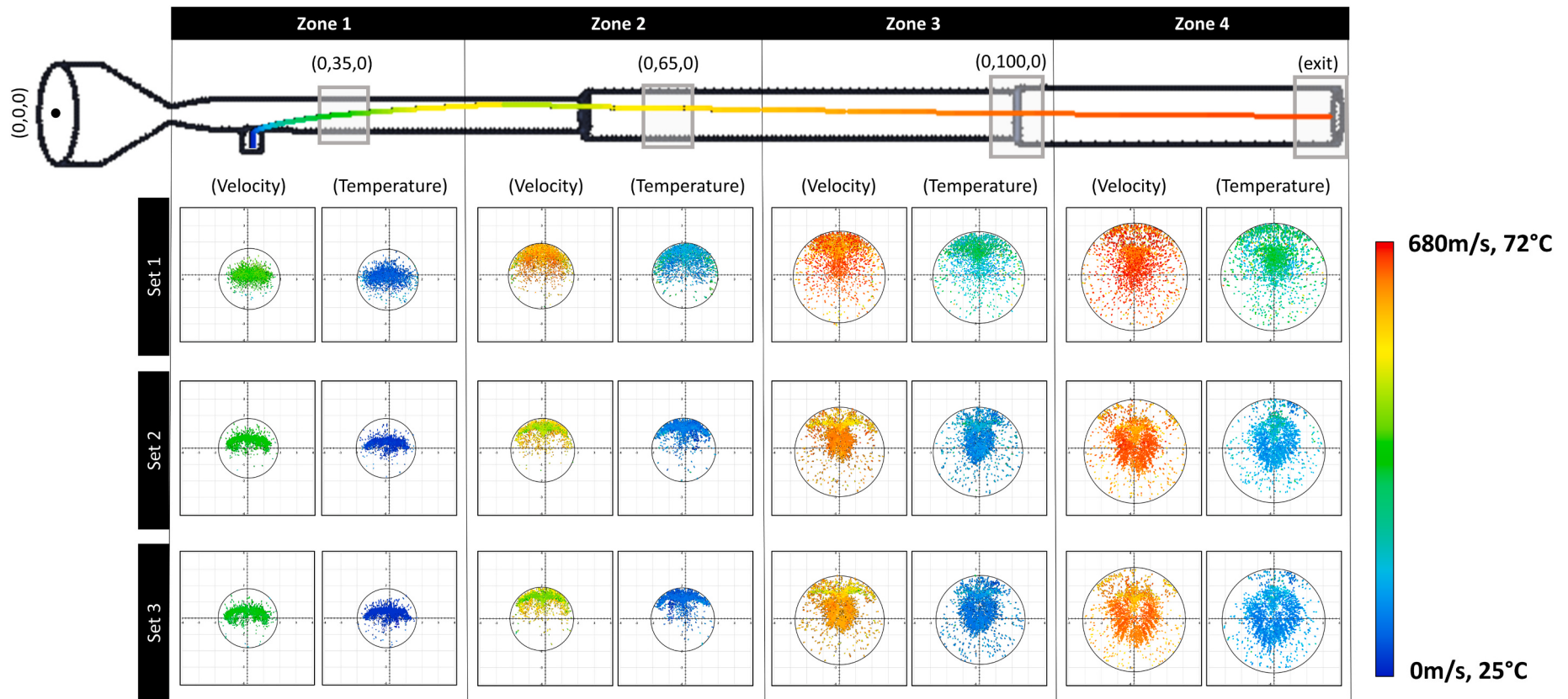


Fig. 6. LPCS particle velocity and temperature from near powder injection location to nozzle exit. Particle radial distribution and spatial temperature and velocity at different locations are provided, i.e. 35 mm (zone 1), 65 mm (zone 2), 115 mm (zone 3) and 147 mm (zone 4) with respect to the set origin (0,0) position. A single in-flight velocity streak line of a 40 μm particle is depicted to demonstrate the effect of nozzle impact on the particle overall momentum.

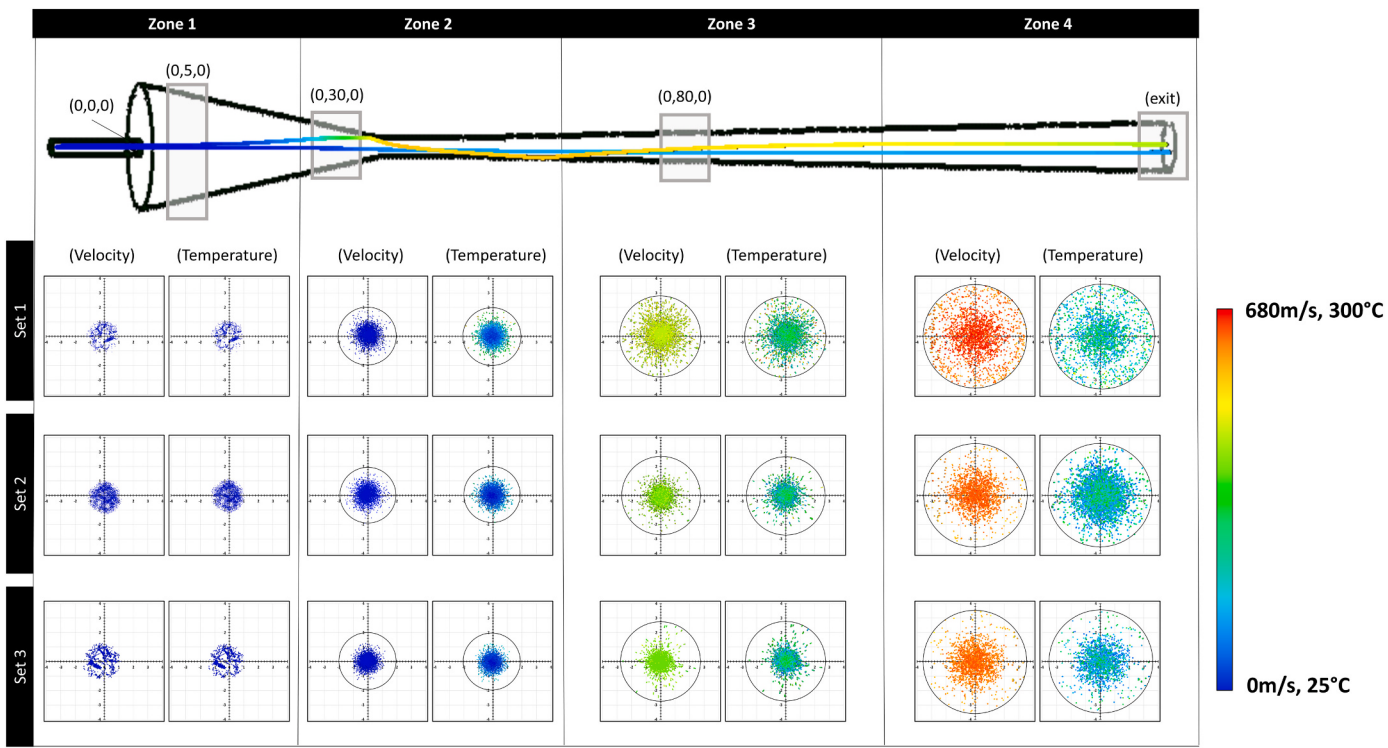


Fig. 7. HPCS particle velocity and temperature from powder injection to nozzle exit. Particle radial distribution and spatial temperature/velocity at different locations are provided, i.e. 5 mm (zone 1), 30 mm (zone 2), 80 mm (zone 3) and 172.5 mm (zone 4) with respect to the set origin (0,0) location. Two particle streak lines, i.e. central cold and hot scatter, of a 40 μm particle are depicted to show the influence of particle spreading in the sonic zone on the in-flight particle exit temperature.

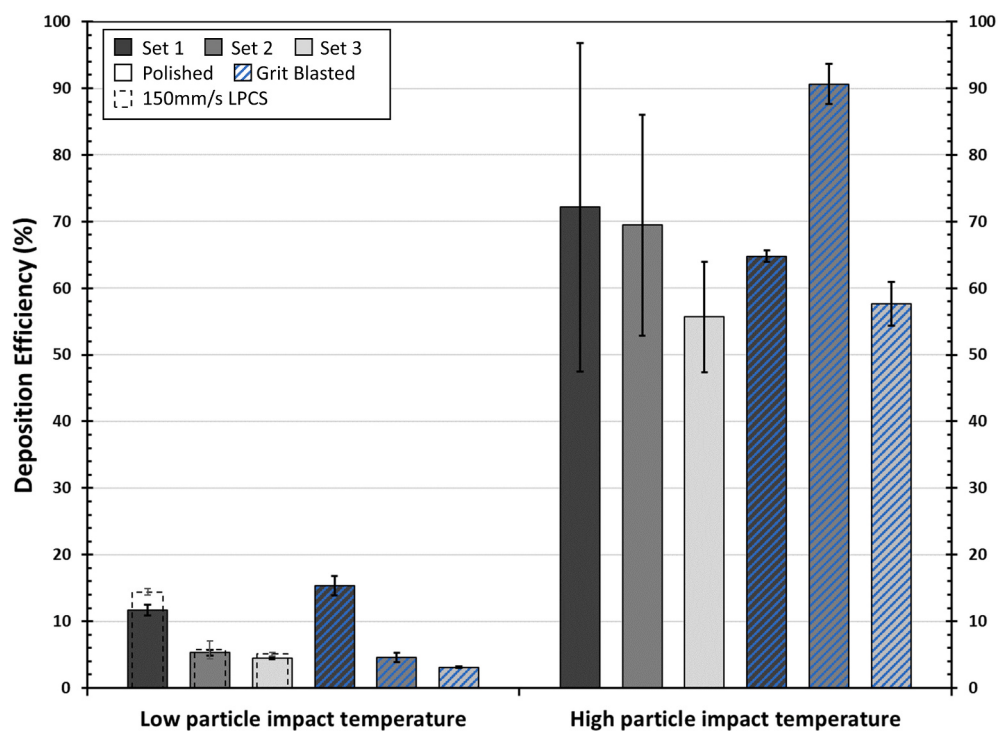


Fig. 8. Coating DE for various particle size range (sets) and substrate surface roughness deposited using both LPIT and HPIT depositions. Data shown as solid fill represents deposits made on polished surfaces while patterns filled data correspond to coatings generated on grit blasted substrates. Superimposed dashed columns in the LPIT represent the DE for coatings sprayed at a gun traverse speed of 150 mm/s on polished surfaces.

5.2. Deposition efficiency

Fig. 8 shows the DE of all deposited aluminum coatings in the current study. For coatings produced with low particle impact temperature (LPIT) using the LPCS system, the DE is low and the particle size noticeably affects it. The feedstock powder set 1 is almost double the DE values obtained for powder set 2 and set 3, i.e. 13% vs ~5%. **Fig. 8** also shows that the CS gun traverse speed has minor influence on the measured DE. A significant improvement in DE is recorded when particle impact temperature is increased with average DEs of 81%, 76% and 57% for powder sets 1, 2 and 3 respectively, which shows a decrease with particle size increase. Finally, the substrate surface roughness with a measured R_a of $6.3 \pm 1.8 \mu\text{m}$ and $0.3 \pm 0.1 \mu\text{m}$ after grit blasting and polishing respectively, expected to affect primarily the deposition of the first layer of particles [68,69], does not influence the overall measured DE in all sprays. The sudden drop in DE of the high particle impact temperature (HPIT), generated using the HPCS system, feedstock set 1 onto the grit blasted sample is believed to be caused due to inconsistent powder feeding resulting from local clogging/deposition inside the nozzle.

Fig. 9 shows the top surface of the produced coatings using both LPIT and HPIT depositions illustrating the effect of different impact dynamics occurring due to particle size and particle impact temperature. LPIT deposits exhibit much smoother coating surfaces as the particles are more deformed, and this effect is enhanced with increasing particle size. The coating top surface features for LPIT depositions generated under both traverse speeds are the same such that only one is shown for conciseness. The top surface of HPIT coatings shows minimal particle deformation upon impact, as seen in **Fig. 9b, d and f**, as the particle original spherical shape is easily detectable.

5.3. Coating adhesion strength

Fig. 10 shows the coatings adhesion/cohesion strength for all sprayed cases. The substrate surface roughness generated using a grit blasting process induces a low adhesion strength irrespectively of particle impact temperature and size. The average adhesion strength on grit blasted surfaces for both low and high particle impact temperatures is $10.9 \pm 4.5 \text{ MPa}$. Similar adhesion strength values have been observed in a previous work with irregularly shaped pure aluminum powder

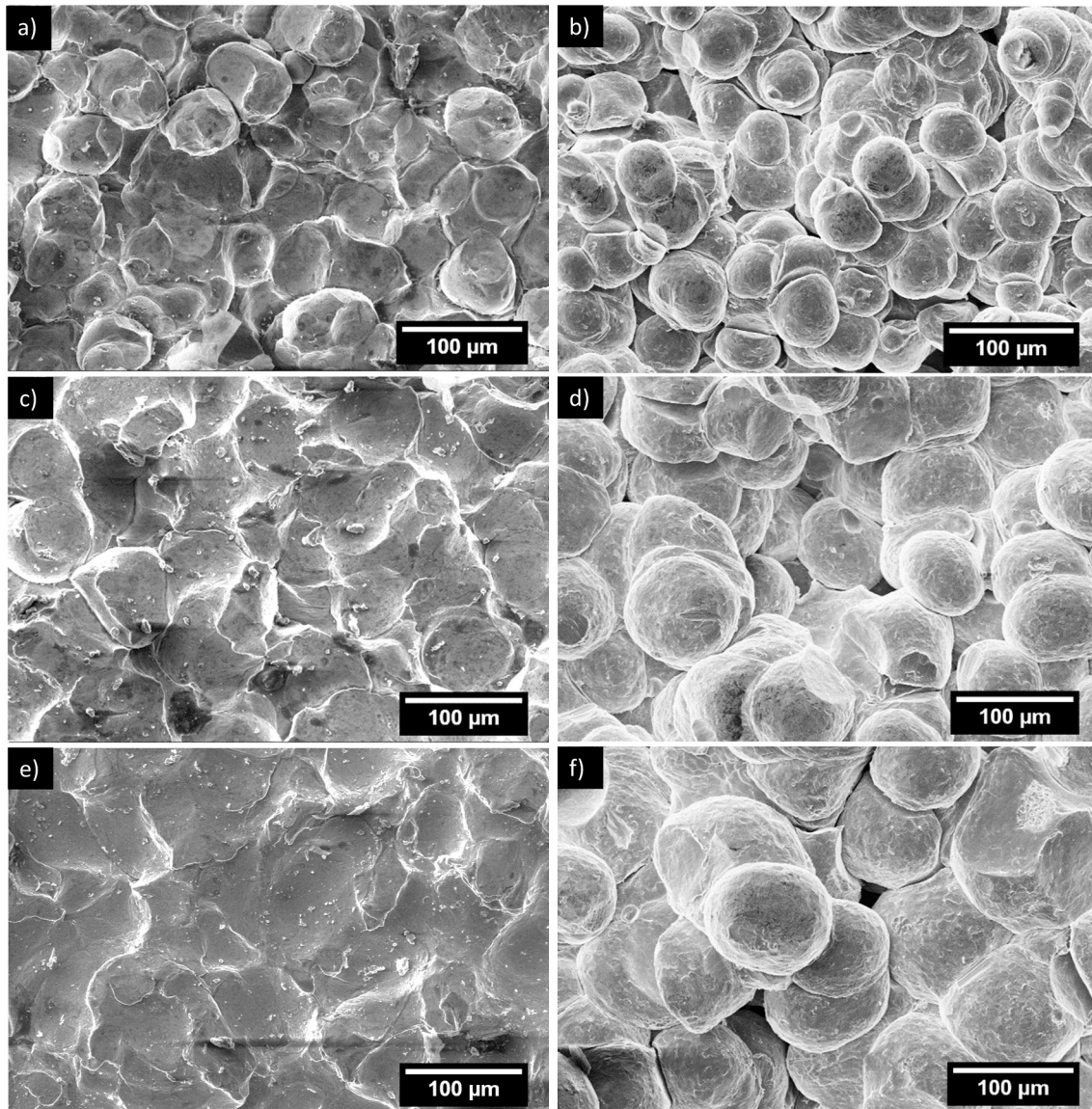


Fig. 9. Coating top surface topography after spray illustrating the contrast in impingement phenomena when utilizing low (left) and high (right) particle in-flight temperatures for powder (a–b) set 1, (c–d) set 2 and (e–f) set 3.

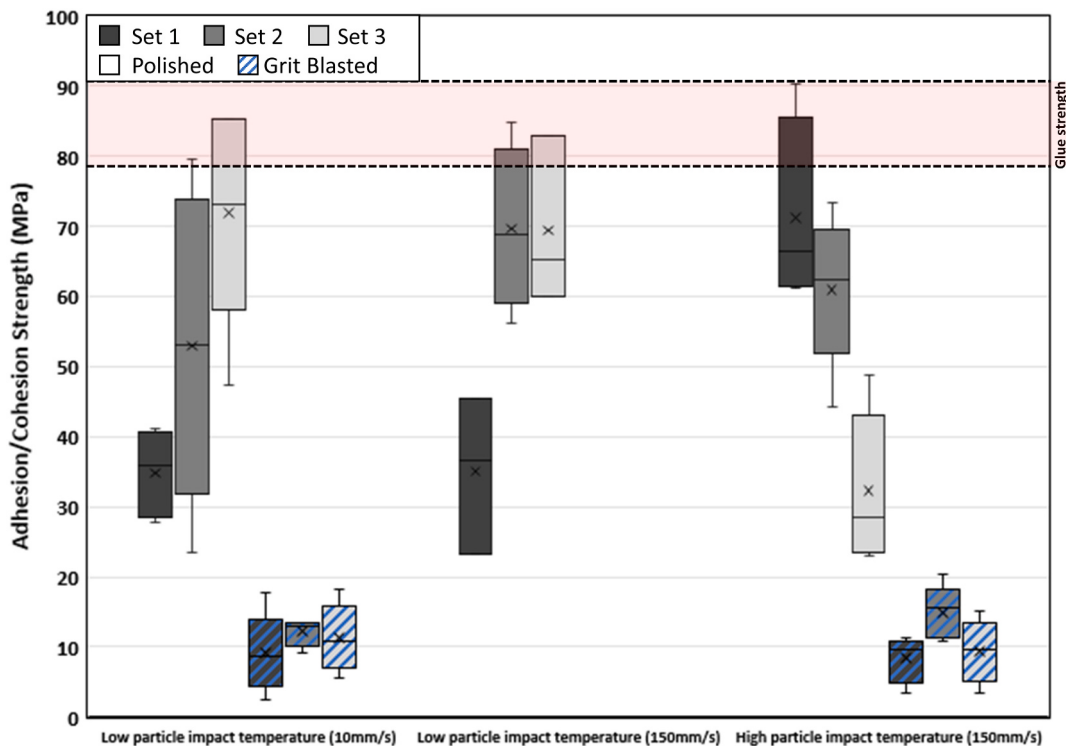


Fig. 10. Coating adhesion/cohesion strength based on particle size (sets 1–3) and substrate roughness for sprays generated using low and high particle impact temperatures. The box shows the position of the 25th percentile, median and 75th percentile. Whisker lines illustrate the data variability outside the upper and lower quartiles while the 'x' marker displays the mean data value. The minimum and maximum values exclude outliers.

material [5].

An increase in coating adhesion strength is observed with the increase of particle diameter for LPIT deposits. The average value increases from 34.8 MPa to 71.7 MPa for set 1 to set 3 powder size sets. The CS nozzle traverse speed for LPIT sprays shows minor influence on the general bond strength trend across all three sets of deposited powders. A decrease in adhesion/cohesion strength is observed with particle size increase for the case of HPIT sprays, from 71.2 MPa to 32.3 MPa for set 3 and set 1 respectively. This trend is the opposite of the one observed for LPIT.

Fracture surface topologies of the pull test sets have also been obtained for deposits made on polished surfaces, as shown in Fig. 11, to characterize the phenomena responsible for coating failure. Imaging of grit blasted surfaces fracture surface topographies was omitted due to the coating consistent low adhesion stress failure. The fracture topology imaging describes the fracture zones by providing the failure location inside the layered pull test set, i.e. glue, coating (cohesion) and/or substrate/coating (adhesion).

Complete coating separation at the interface is detected for all sets sprayed using LPIT at a traverse speed of 10 mm/s, as shown in Fig. 11a–c. The coatings, irrespective of particle size and unrelatedly to the recorded bond strength, fail in complete adhesion. As shown in Fig. 11a–c, the substrates surfaces after adhesion tests retained their mirror finish polish i.e. observable through the reflective surface feature, indicating that the recorded adhesion failures primarily involve metallic bonding and lack mechanical anchoring. Coatings sprayed at LPIT and at a traverse speed of 150 mm/s display a similar complete coating separation from the substrate surface, with limited residual aluminum particles, for powder set 1. However, local adhesion fracture is observed for powder set 2–3, as seen in Fig. 11e–f.

Finally, localized irregular adhesion fracture is seen for coatings deposited with HPIT, as depicted in Fig. 11g and h. Powder set 3, however, characterized with the lowest bond strength, failed in a mixed adhesion/cohesion process. This rupture nature is observed on the entire

substrate surface, which excludes distinctive localized fracture developments.

5.4. Bend-to-break tests and fractography

As shown in Fig. 12a, coatings generated using LPIT sustain large deformations prior to crack initiation and eventual full propagation, suggesting high apparent ductility. Prior to failure, tested coatings had to be bent multiple times to initiate fracture. HPIT coatings, on the other hand, broke abruptly, as shown in Fig. 12b–c, with limited crack deflection and at restricted curvature.

The resulting fracture surfaces from the bend-to-break tests are shown in Fig. 13. The LPIT coating fracture surfaces show presence of very irregular and jagged features, representative of highly impinged particle network, enhanced particle to particle contact, fish scale particle-particle architectural arrangement and some level of intra-particle fracture. For the HPIT samples, the fracture surfaces exhibit a prevailing inter-particle crack propagation route, leading to a smooth path characteristic of the highly noticeable spherical particle geometry.

6. Analysis and discussion

The current section provides a detailed analysis of the numerical and experimental results to associate generated coating properties and characteristics to particle impact temperature and size. A deeper look into the numerical work offers a statistical view of particle impact characteristics, dependent on flow trajectory and size, necessary for successful deposition and improved adhesion.

6.1. Deposition efficiency and critical velocity (V_C)

The influence of particle impact temperature and size as well as substrate state on DE and V_C are presented in the current sub-section.

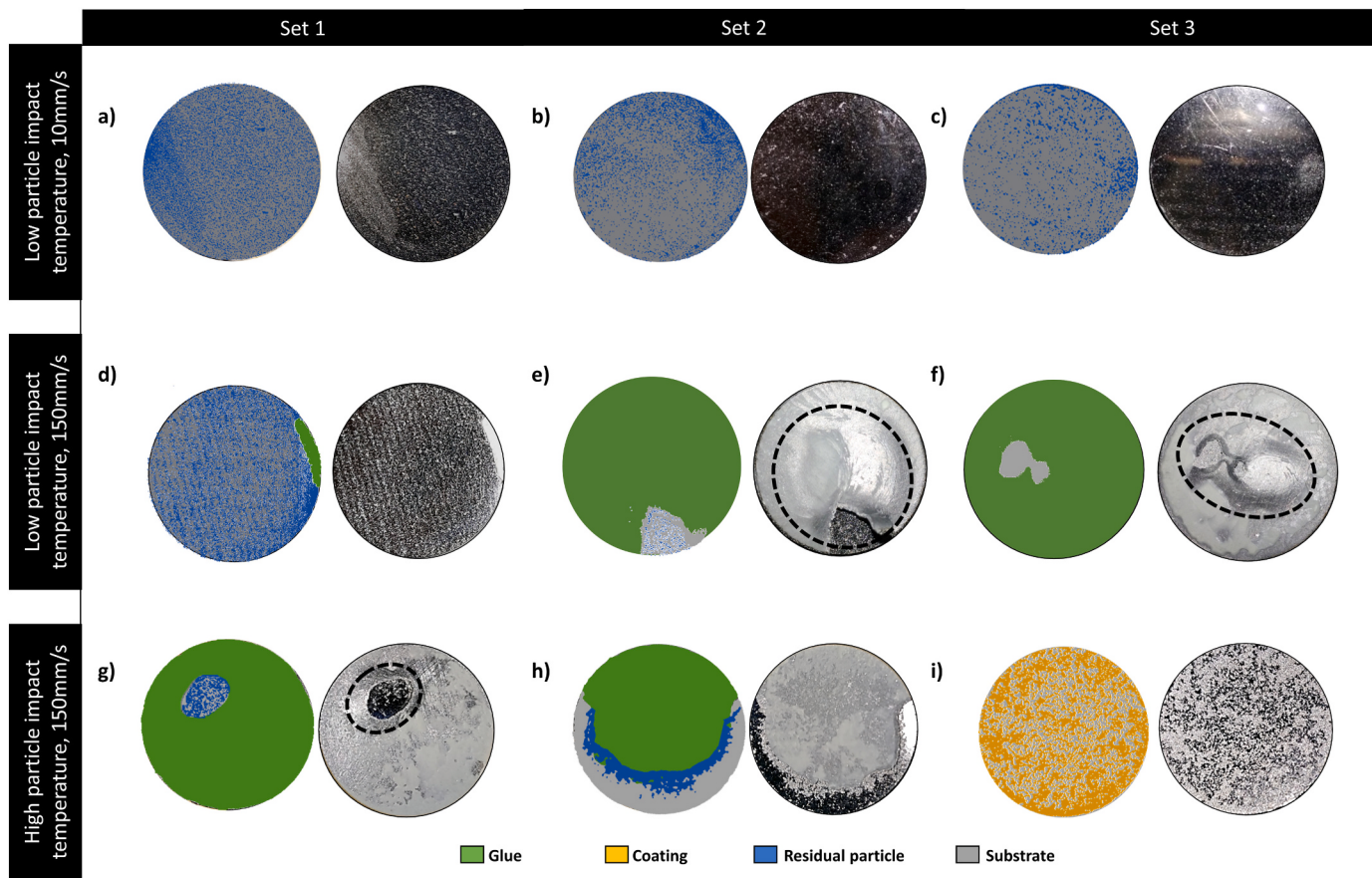


Fig. 11. Representative failure features after pull test of the substrate side only. For each case, the right image shows the actual state of the coated substrate surface after pull test while the left provides distinction between different zones on the same substrate side using a color code, which is defined in the legend. The resulting strength at failure for each shown case (and corresponding particle size set) is a) 40 MPa (set 1), b) 68 MPa (set 2) and c) 74 MPa (set 3), d) 45 MPa (set 1), e) 67 MPa (set 2) and f) 72 MPa (set 3), g) 70 MPa (set 1), h) 65 MPa (set 2), i) 49 MPa (set 3). Dotted lines delineate zones of protruding coating. (For interpretation of the references to color in this figure legend, the reader is referred to the web version of this article.)

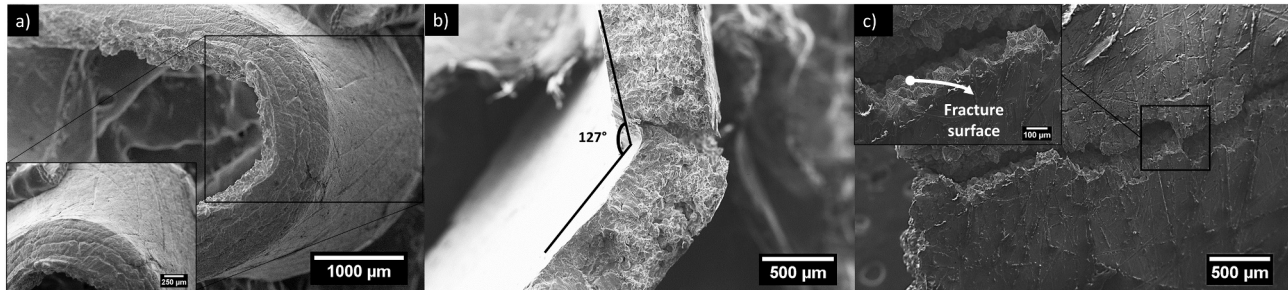


Fig. 12. SE SEM images of coatings during the bend-to-break process using feedstock powder set 2 with a) LPIT deposits showing no sign of cracking during the first phase of the bend-to-break test and b–c) HPIT deposits. A fracture surface from the HPIT coating is highlighted in image c).

6.1.1. Particle temperature influence

It is seen from Figs. 6 and 7 that the spray parameters and nozzle configurations used allowed reaching LPITs (around 50 °C) and HPITs (above 200 °C) for similar particle impact velocity, for each feedstock powder set. This increase in particle temperature facilitates dislocation motion such as climbing and cross-slip, enabling dislocation-based material softening, enhancing particle deformation, increasing local heating, with potentially larger interfacial regions reaching $0.5T_{\text{melting}}$ due to the conversion of kinetic energy into heat during the impact process and improving oxide layer fracture and removal processes [36,37,70]. Altogether, these effects increase fresh metal surface contact available for bonding and decrease V_C [37,39], which results in the increase of DE

for high particle impact temperature cases, seen in Fig. 8, for the three feedstock sets compared to the cases of LPIT.

Detailed analysis of the data from Figs. 6 and 7 allows generating a statistical particle velocity distribution for each tested case, shown in Fig. 14. To capture the actual powder size distribution, particles have been selected randomly from each size range following the measured number distribution percentage. A total of 10,000 particles have, thus, been used for each analyzed powder set.

The results show similar overall particle velocity distribution trends and average particle velocity between both particle impact temperatures for all three sets of powders. The V_C values for each case have been obtained from Fig. 14 data by grouping fastest particles together until

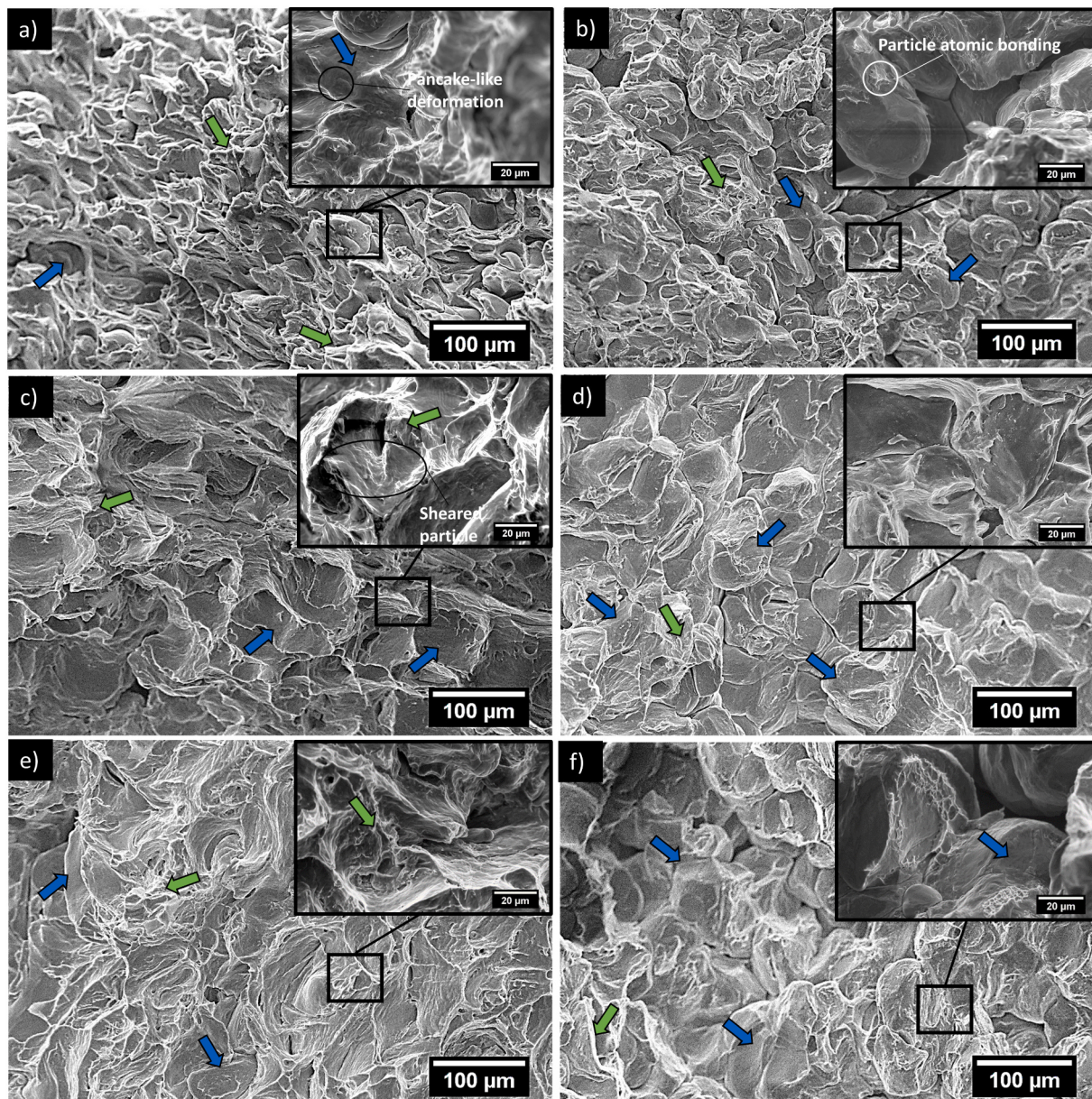


Fig. 13. Fracture surfaces from the bend-to-break tests for coatings generated with low (left) and high (right) particle impact temperatures. Shown coatings correspond to (a–b) set 1, (c–d) set 2 and (e–f) set 3. Blue arrows point to zones of inter-particle separation and green arrow indicate presence of intra-particle failure. (For interpretation of the references to color in this figure legend, the reader is referred to the web version of this article.)

their amount percentage over the overall particle population matched the measured DE [36]. The slowest particle velocity in these grouped particle population was chosen as the corresponding V_C of the studied powder set. Fig. 14 highlights, i.e. in black and green, all particles traveling faster than the critical velocity evaluated for each case, while Table 4 summarizes the obtained V_C values. The increase of particle impact temperature results in a decrease of V_C for each powder set, as suggested by theoretical models that predict a decrease in V_C as particle impact temperature increases [71].

6.1.2. Particle size effect

The particle native oxide layer thickness and oxide content can influence V_C and thus DE. The thicker the oxide layer, the more kinetic energy is required to break and remove this shell, reducing the energy available for particle and substrate plastic deformations that lead to bonding. Particle oxygen content was detected through inert gas fusion method for the current particle sets. Assuming that the oxygen content is

solely associated to the surface oxide, it was found that this layer decreased from 15.4 ± 3.3 nm for powder set 1 to 10.2 ± 2.8 nm for particle set 3 [72], which can also be used to partially explain the V_C observed reduction with particle size. If the oxygen content originates from oxygen inclusions present at grain boundaries, it is expected that the oxide-dispersion strengthening process during deformation will be of less consequence for larger particle size due to the lower oxide concentration in larger particle volumes, leading again to a lower V_C as particle size increases. This size dependent influence on V_C is more easily demonstrated for LPIT as the impact temperature remains low and almost constant for all three particle sets, thus only the diameter is changed. It is observed that particle V_C decreases with increasing particle size.

Fig. 8 shows that the measured DE of all coatings decreases with particle size. As particle size increases, Fig. 14 shows that the velocity distribution shifts towards slower speeds, following approximately the relation $V_p \propto d^{-1/2}$ given between particle velocity vs particle diameter

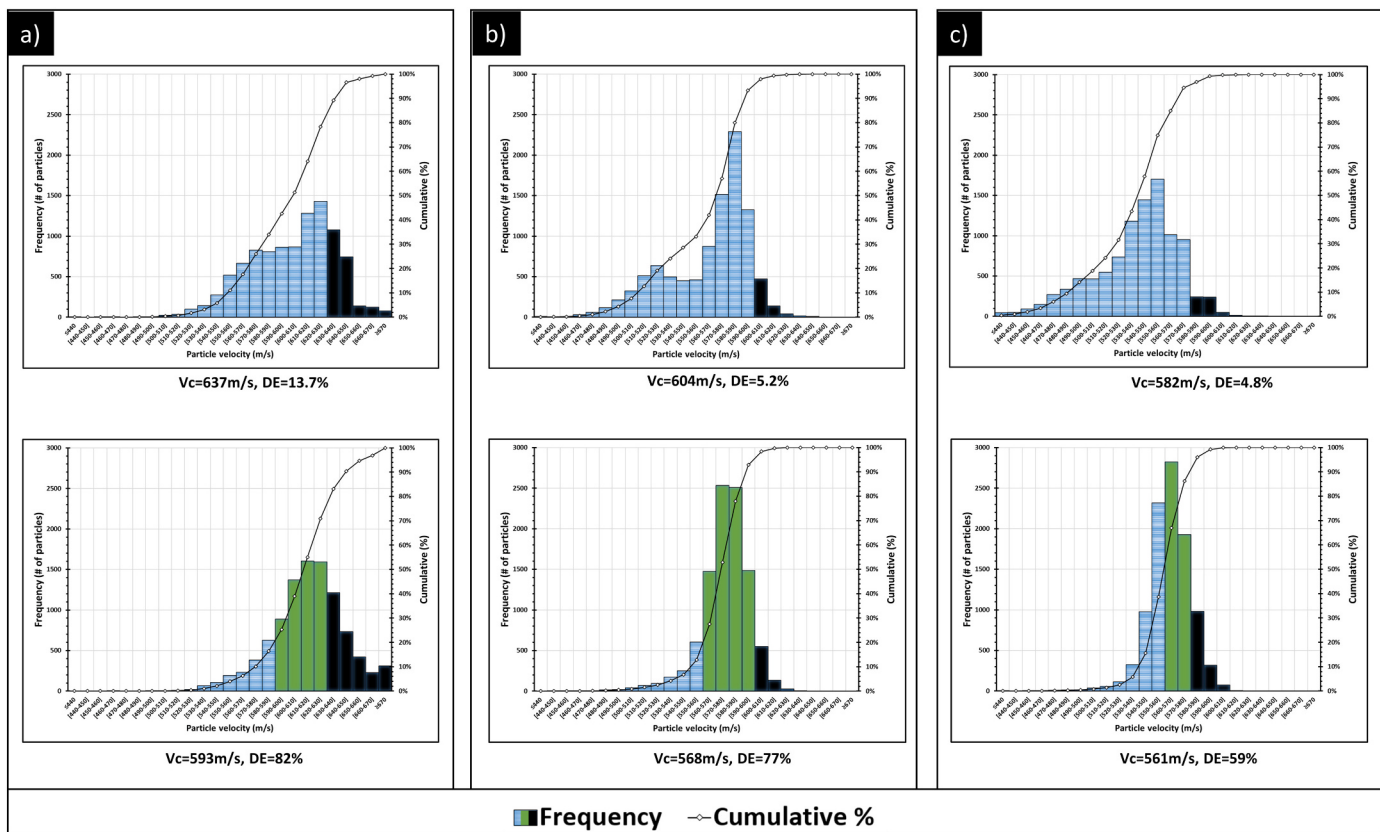


Fig. 14. Model results of particle velocity distribution and cumulative sum at the nozzle exit for 10,000 representative particles from a) set 1, b) set 2 and c) set 3. Top and bottom row refer to deposits generated with LPIT, through the LPCS system, and HPIT, through the HPCS, respectively. In black: particles traveling above the LPIT V_c . In green: particles traveling at HPIT V_c . In blue: particles traveling below their respective V_c . V_c are evaluated based on experimental DE measurements. Corresponding numerical V_c and DEs are indicated for each powder set. (For interpretation of the references to color in this figure legend, the reader is referred to the web version of this article.)

Table 4
 V_c for all three powder sets and both low and high particle impact temperature.

Powder size	Set 1 ($\phi_{average} = 40$ μm)	Set 2 ($\phi_{average} = 53$ μm)	Set 3 ($\phi_{average} = 63$ μm)
LPIT V_c	637 m/s	604 m/s	582 m/s
HPIT V_c	593 m/s	568 m/s	561 m/s

[72]. This results in lower DE despite the reduction of V_c associated with larger particle size as the particle impact velocity decreases more rapidly than its V_c .

6.1.3. Substrate surface state influence

6.1.3.1. Roughness. The substrate surface roughness, which mostly affects the first layer of deposited material, shows no influence/trend on measured DE, as presented in Fig. 8. If any, the effects, which would take place only at the interface between the first particle layer and substrate, are being suppressed by the overall averaging process involved in DE measurement. Analogously, the V_c determined from Fig. 14 is almost inclusively the V_c amongst the CS aluminum particle layers, which also disregards the influence of substrate surface properties. However, due to the harder nature of the steel substrate in comparison to the CS aluminum, the V_c values of the first impinging particles are expected to be lower than the reported numerical values in the current study [71,73].

6.1.3.2. Temperature. The substrate temperature in the current study has been indirectly varied by adjusting the gun traverse speed in the

LPCS system to induce varying gas/substrate impact interaction times. Based on obtained results shown in Fig. 8, the substrate temperature shows no significant influence on measured DE. This can be associated to the DE measurement averaging process and/or limited instant local surface temperature rise the change in gun traverse speed generates and/or restricted heat transfer processes it produces across the interface. As the most probable and substantial cause is related to the DE measurement process, actual local temperature effects can be present. If any, the effects of temperature rise, through gun traverse speed modifications, on V_c are twofold. A temperature rise can enhance substrate deformation during impact, which can promote proper substrate oxide fracture and removal resulting in a decrease of V_c . In addition, the increase in temperature and extended jet time from decreased gun traverse speed can also improve surface cleaning processes i.e. organic debris, permitting proper fresh-metal contact for eventual bonding. On the other hand, substrate surface temperature rise can likewise increase V_c from possible substrate oxide scale growth during the cooling process within the atmospheric environment occurring once the hot supersonic nitrogen stream leaves the substrate surface. As the growth of an oxide scale has a direct measurable impact on adhesion, this possible influence of temperature will be verified and discussed in the next section.

6.2. Adhesion strength

While the DE and V_c can simply be defined based on a binary “successful vs unsuccessful” deposition criteria, the coating properties such as adhesion strength account for the variety of particle impact characteristics. This is particularly the case for the HPIT cases in which a large population of particles with different impact characteristics achieves

successful deposition while only a limited collection does deposit in the case of LPIT as revealed by the lower DE. This breadth of particle impact characteristics is expected to affect the coating overall structure and adhesion.

The particle impact characteristics variance is presented in Fig. 15, which illustrates the particle population at the nozzle exit reaching speeds above V_C , from the particle streak results presented in Section 4.2. One can observe that the particles spread for the LPIT case corresponds well with the experimental single spot sprays (nozzle not moving) included in Fig. 15a and c for set 1 and set 3 respectively. This dispersion confirms the departure of particle distribution from stream symmetry and attests skewed particle size dependent trajectory. In the HPIT cases, the particle spread includes a clear high particle concentration at the nozzle center and a gradual decrease in particle stream density following a Gaussian-like distribution, as most commonly observed in CS depositions [74]. In addition to all particles reaching warmer temperatures than in LPIT cases, a large temperature distribution is also detected for all three sets.

6.2.1. Particle temperature effect

For a set particle diameter, V_C can vary significantly as the impact particle temperature can fluctuate from one particle to another based on their in-flight history. To relate particle impact characteristics to the inherent individual particle V_C , the following expression is used for material impacting on the same material [75]:

$$V_c = k_1 \sqrt{c_p(T_m - T_p) + 16 \frac{\sigma}{\rho_p} \left(\frac{T_m - T_p}{T_m - 293} \right)} \quad (16)$$

where T_m is the particle melting temperature, T_p is the particle impact temperature, σ is the tensile strength of the particle material at 293 K, k_1 is a particle size-dependent fitting parameter and c_p is the specific heat of the particle material. To find the size-dependent dimensionless fitting parameter, k_1 , the LPIT characteristics have been utilized as their temperature has been found to be very similar for all particle size range. The T_p term has been taken as the average particle exit temperature and V_C as the numerically calculated V_C of each powder set. The resulting particle size dependent fitting parameters are 0.56, 0.59 and 0.62 for powder sets 1, 2 and 3 respectively, which fits within the range anticipated during the development of Eq. (14) [75].

Using these values of k_1 , the dimensionless parameter $\eta = V / V_C$ is used to qualitatively evaluate the extent at which each particle exceeds its inherent V_C for each deposited feedstock set and for both LPIT and HPIT cases. The results are outlined in Fig. 16 using a box and whisker plot in which the quartile calculation excludes the median and upper outliers. For particles impacting on the same material, larger η values would lead to larger adhesion/cohesion strengths [75], but this is not always the case for the adhesion of dissimilar materials [76]. In the current work, since all studied conditions generate a minor substrate deformation compared to the particle, the provided trends in Fig. 16 are considered representative. However, no quantitative significance is given to values of η as the overall influence of substrate nature on deposition is disregarded in both the current calculated V_C values and Eq. (14).

One can observe that for the same feedstock set and for both LPIT and HPIT cases, the average value of η is slightly larger for the latter case, as a result of the increased particle impact temperature. One should expect the HPIT cases to exhibit larger adhesion/cohesion strengths than their low particle temperature counterparts that were sprayed at the same impact velocity but lower η . Although only the effect on cohesion has been recorded through powder set 3 measured strength, it is expected that both powders set 1 and set 2 follow the trend despite the glue failure and consequently unknown actual adhesion strength.

However, this expected trend is not observed. This suggests that the adhesion strength might be governed by other factors than solely by those included in the η parameter. It is anticipated that the extensive in-

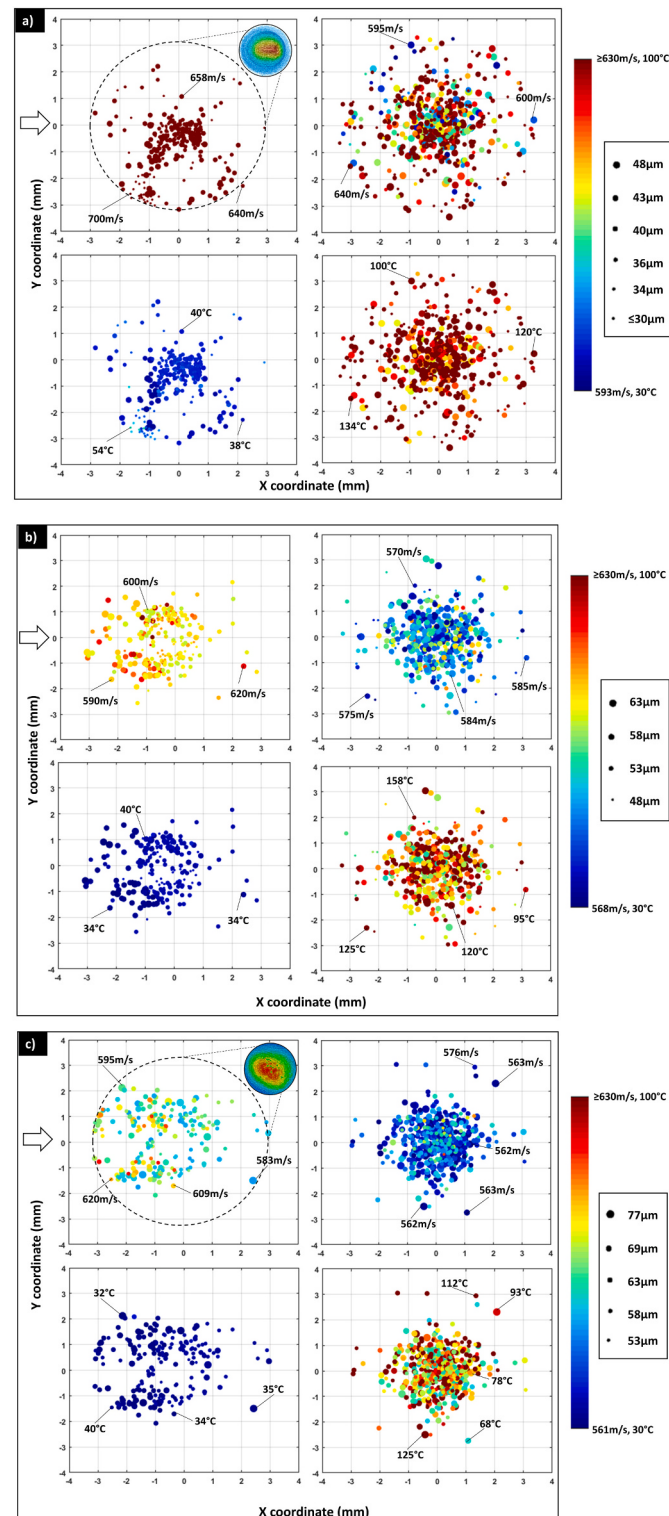


Fig. 15. Particle spread colored based on local particle velocity (top) and temperature (bottom) for the low (left) and high (right) particle impact temperature deposits, and for a) set 1, b) set 2 and c) set 3. Particle individual size, within each set, is illustrated by varying the representative dot dimensions. The powder injection in the LPIT is oriented from the negative-x axis towards the origin as demonstrated by the included arrows. Insets of experimental LPIT spot spray deposits are incorporated to additionally demonstrate the simulation result accuracy.

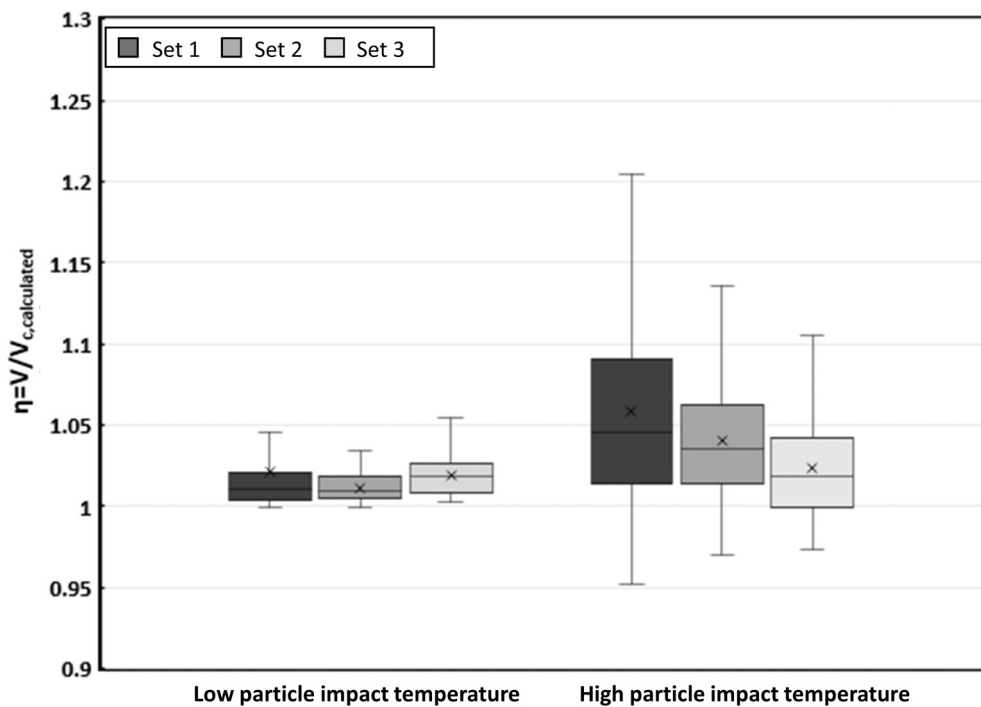


Fig. 16. Particle $\eta = V / V_c$ for all three sets of feedstock powder and for deposits generated at varying particle in-flight temperature. The minimum and maximum values exclude outliers.

situ hammering as a result of low DE for the LPIT cases must govern the adhesion/cohesion results for these three sets. Bouncing off particles provide significant in-situ hammering/shot peening to increase the deformation of deposited particles, improve the oxide film removal through shear and enhance interfacial fresh metal contact pressure of particles adhered to the substrate surface, all of which are considered factors contributing to adhesion. The results also suggest a particle impact temperature threshold under which impingement becomes the primary factor governing adhesion/cohesion strength.

6.2.2. Particle size effect

For the LPIT cases, an increase in bonding strength with an increase in particle size is observed and is associated primarily to the decrease of DE with particle size, which enhances the impingement effect as previously explained. In addition, the slower cooling rates associated with larger particles following deposition can lessen thermal stresses and shrinkage related local in-situ de-bonding processes, favoring developments and subsistence of atomic bonding [77]. For the HPIT cases, the influence of particle size on adhesion is associated to both the particle size dependent impact temperature and velocity. As observed in Fig. 15, an increase in particle size leads to an important drop in temperature and velocity distribution, which together lower the particle population capable of exceeding velocities well above their V_c , i.e. reduced η , leading to the observed reduction in adhesion with particle size. Analogously, the inter-particle cohesion strength is also expected to decrease with decreasing η values, which is shown to occur in the current study as the coating fracture mode shifts from adhesion (set 1 and set 2) to a mixture of cohesion/adhesion (set 3) with increasing size, as shown in Fig. 11g–h–i.

6.2.3. Substrate surface state influence

6.2.3.1. Roughness. The low coating adhesion strength of LPIT cases on grit blasted surfaces, as presented in Fig. 10, is associated to the substrate topography influence on particle deformation. The roughened surface restricts material flow localization, heat generation and contact

pressure, which deprives the interface of processes required for the generation of strong metallic bonds [44]. In addition, rough surface profiles can trap disrupted oxide film residues serving directly as a barrier to fresh-metal contact [44]. Since the same adhesion trend is observed for the HPIT cases, it can be hypothesized that the η parameter values reached in the current study are insufficient to alter the contact processes. Provided that the adhesion values fall below 20 MPa, the coating connection onto the substrate results predominantly, if not entirely, from mechanical anchoring [44].

6.2.3.2. Temperature. In the LPIT deposits, the powder set 1 and set 2 minor adhesion decline as the traverse speed is decreased to 10 mm/s, might be associated to an oxide scale growth process rendering direct fresh metal contact difficult. As discussed in Section 6.1.3, the oxide growth can result from the substrate surface exposure to the environment after being heated by the impacting supersonic gas flow at low traverse speed. This oxide film influence is inclined to be more noticeable for smaller particle size as they travel at lower E_k alongside an initially larger native oxide film. On the other hand, since the HPIT deposits have been generated at the highest gun traverse speed, i.e. 150 mm/s, and that the observed wall jet radial flow and recirculating stagnation zone are found to be at much colder temperatures than in the LPCS system, it is evident that the substrate temperature effects, if any, are diminished. Consequently, all measured coating bonding strength outcomes reflect predominantly the exposed particle characteristics influence on adhesion, which is also in agreement with the previously proposed conclusions provided in Section 6.2.1.

6.2.4. Crack propagation mechanisms

Although LPIT deposits sprayed at 10 mm/s and 150 mm/s undergo similar in-situ peening processes and reach overall comparable bonding/failure strengths, they undergo dissimilar fracture processes, as shown in Fig. 11 in which the powder set 2–3 present a predominant glue failure when sprayed at 150 mm/s. Due to the low DE under which both coatings are deposited, general microstructural features such as pancake-like particle-particle deformation, presence of mechanical

anchoring at particle junctions and intermingled particle splat contact area are expected to exist in both deposits. Neglecting impact associated recrystallisation feature dissimilarities, the different fracture processes can be linked to the dissimilar thermal history/in-situ annealing associated with gun traverse speed and to the different number of deposit layers utilized. Lack of a complete microstructural evaluation, however, restricts the confirmation of the exact impact related phenomena that lead to the dissimilar fracture surfaces in both LPIT depositions.

For the HPIT cases, the limited in-situ peening process inherent to the high DE restricts particle deformation as observed in Fig. 9. The coating cohesion failure, recorded for powder set 3 and shown in Fig. 11i confirms the significance of particle-particle boundary characteristics, associated to the η value under which deposition occurs, and the presence of preferable low energy crack propagation paths on coating strength and effective properties. Powder set 1 and set 2 exhibit increased particle-particle cohesion strength due to their depositions under larger η parameter, resulting in a localized coating fracture rather than a cohesive failure or full adhesion separation.

6.3. Bend-to-break tests

The improved apparent ductility of the LPIT coatings, observed in Fig. 12a, can be attributed to the presence of crack blunting, crack deflection mechanisms and/or particle-particle fish scale structural effect [78] serving to distribute the deformation, mitigate stress concentration and provide pseudo-plasticity, i.e. deformation facilitated by particle boundary sliding [78,79]. These mechanisms related to the particle microstructural arrangement resulting from the high level of in-situ peening, lead to the irregular fracture surface depicted in Fig. 13.

For the HPIT coatings, despite the larger η values compared to the LPIT deposits, the reduced apparent ductility and brittle fracture occurring during the bend-to-break tests, as shown in Fig. 12b–c, are attributed to increased cohesion bonding that limits the fish scale effect. Recognizing that a crack path propagates along the easiest low-energy route, existing porosity and microcracks may all lead to premature fracture of the tested samples. The fracture surface of a fast growing and propagating crack, in a particle network, theoretically shows limited material deformation and fragmentation, original particle surface features and overall low coating bending ability, which is observed in the fracture surfaces of Fig. 13.

7. Conclusions

The current work studied the influence of pure aluminum particle impact temperature, i.e. colder vs warmer particles, for a given particle size, on steel substrate cold spray deposition and coating properties, using both experimental and modeling results. The following conclusions are drawn:

For sprays characterized by colder particle impact temperature

1. The DE is low (below 10%) for all particle size ranges, as most particles do not experience sufficient deformation upon impact with the substrate to achieve bonding. The DE decreases with increasing particle size as the reduction of their impact velocity is not compensated by the decrease of their critical velocity.
2. The coating adhesion strength increases drastically with particle size, under constant η depositions, as a result of the severe in-situ hammering processes induced by decreasing DE with particle size.
3. The in-situ shot-peening also leads to the formation of important fish scale effect, which provides the coating with pseudoplasticity and apparent ductility.

For sprays characterized by warmer particle impact temperature

1. The DE is large (above 60%) due to sufficient particle deformation upon impact with the substrate, promoted by the warmer particle

impact temperature. The DE decreases with particle size as their decrease in impact velocity is not counterbalanced by their decline in critical velocity.

2. The coating adhesion/cohesion strength decreases with particle size and is governed by the non-dimensional parameter η . Despite their intrinsically increasing V_C , smaller particles reach much higher impact temperatures, which sufficiently decreases their V_C , and much higher impact velocity due to their lower mass. With increasing particle size and constant gas stagnation parameters, larger particles are inherently heated to lower temperatures, which are sufficient to increase DE from room temperature impact deposition but observed to be consequently detrimental for cohesion processes.
3. Higher particle cohesion related to high η values limit fish-scale like effects during deformation. However, the high level of defects (porosity, unbonded areas) lead to brittle-like fracture characterized by a straight crack trajectory.

Declaration of competing interest

The authors declare that they have no known competing financial interests or personal relationships that could have appeared to influence the work reported in this paper.

Acknowledgements

This project was funded by the Government of Canada. The authors would like to acknowledge the work of the technical officer's team in Boucherville: K. Bricault, F. Belval, P. Dionne and C. Hoang.

References

- [1] N. Sanpo, M.L. Tan, P. Cheang, K.A. Khor, Antibacterial property of cold-sprayed HA-ag/PEEK coating, *J. Therm. Spray Technol.* 18 (2009) 10–15, <https://doi.org/10.1007/s11666-008-9283-0>.
- [2] H. Che, X. Chu, P. Vo, S. Yue, Cold spray of mixed metal powders on carbon fibre reinforced polymers, *Surf. Coatings Technol.* 329 (2017) 232–243, <https://doi.org/10.1016/j.surcoat.2017.09.052>.
- [3] M. Yamada, H. Isago, H. Nakano, M. Fukumoto, Cold spraying of TiO₂ photocatalyst coating with nitrogen process gas, *J. Therm. Spray Technol.* 19 (2010) 1218–1223, <https://doi.org/10.1007/s11666-010-9520-1>.
- [4] H. Katanoda, M. Fukuhara, N. Iino, Numerical study of combination parameters for particle impact velocity and temperature in cold spray, *J. Therm. Spray Technol.* 16 (2007) 627–633, <https://doi.org/10.1007/s11666-007-9087-7>.
- [5] A. Nastic, M. Vijay, A Tieu, S Rahmati, B Jodoin, Experimental and numerical study of the influence of substrate surface preparation on adhesion mechanisms of aluminum cold spray coatings on 300M steel substrates, *J. Therm. Spray Technol.* 26. doi:<https://doi.org/10.1007/s11666-017-0602-1> (n.d.).
- [6] Y. Cormier, P. Dupuis, B. Jodoin, A. Ghaei, Finite element analysis and failure mode characterization of pyramidal fin arrays produced by masked cold gas dynamic spray, *J. Therm. Spray Technol.* 24 (2015) 1549–1565, <https://doi.org/10.1007/s11666-015-0317-0>.
- [7] S. Yin, X. Wang, W. Li, H. Liao, H. Jie, Deformation behavior of the oxide film on the surface of cold sprayed powder particle, *Appl. Surf. Sci.* 259 (2012) 294–300, <https://doi.org/10.1016/JAPSUSC.2012.07.036>.
- [8] M. Hassani-Gangaraj, D. Veysset, K.A. Nelson, C.A. Schuh, Impact-bonding with aluminum, silver, and gold microparticles: toward understanding the role of native oxide layer, *Appl. Surf. Sci.* 476 (2019) 528–532, <https://doi.org/10.1016/JAPSUSC.2019.01.111>.
- [9] P.C. King, S.H. Zahiri, M. Jahedi, Microstructural refinement within a cold-sprayed copper particle, *Metall. Mater. Trans. A Phys. Metall. Mater. Sci.* 40 (2009) 2115–2123, <https://doi.org/10.1007/s11661-009-9882-5>.
- [10] Y. Sheng, C.J. Lawrence, B.J. Briscoe, C. Thornton, Numerical studies of uniaxial powder compaction process by 3D DEM, in: *Eng. Comput. (Swansea, Wales)*, 2004, pp. 304–317, <https://doi.org/10.1108/02644400410519802>.
- [11] L. Tan, Y. Li, F. Liu, Y. Nie, L. Jiang, Microstructure evolutions of a powder metallurgy superalloy during high-strain-rate deformation, *J. Alloys Compd.* 789 (2019) 506–517, <https://doi.org/10.1016/j.jallcom.2019.03.080>.
- [12] Y. Xiong, K. Kang, G. Bae, S. Yoon, C. Lee, Dynamic amorphization and recrystallization of metals in kinetic spray process, *Appl. Phys. Lett.* 92 (2008), 194101, <https://doi.org/10.1063/1.2928218>.
- [13] W.-Y. Li, C. Zhang, X.P. Guo, G. Zhang, H.L. Liao, C. Coddet, Deposition characteristics of Al-12Si alloy coating fabricated by cold spraying with relatively large powder particles, *Appl. Surf. Sci.* 253 (2007) 7124–7130, <https://doi.org/10.1016/JAPSUSC.2007.02.142>.

- [14] A. Nastic, B. Jodoin, Evaluation of heat transfer transport coefficient for cold spray through computational fluid dynamics and particle in-flight temperature measurement using a high-speed IR camera, *J. Therm. Spray Technol.* 27 (2018) 1491–1517, <https://doi.org/10.1007/s11666-018-0787-y>.
- [15] X.J. Ning, Q.S. Wang, Z. Ma, H.J. Kim, Numerical study of in-flight particle parameters in low-pressure cold spray process, *J. Therm. Spray Technol.* 19 (2010) 1211–1217, <https://doi.org/10.1007/s11666-010-9548-2>.
- [16] W.-Y. Li, H. Liao, H.-T. Wang, C.-J. Li, G. Zhang, C. Coddet, Optimal design of a convergent-barrel cold spray nozzle by numerical method, *Appl. Surf. Sci.* 253 (2006) 708–713, <https://doi.org/10.1016/j.apsusc.2005.12.157>.
- [17] R.N. Raeelison, L.L. Koithara, S. Costil, C. Langlade, Turbulences of the supersonic gas flow during cold spraying and their negative effects: a DNS CFD analysis coupled with experimental observation and laser impulse high-speed shadowgraphs of the particles in-flight flow, *Int. J. Heat Mass Transf.* 147 (2020), <https://doi.org/10.1016/j.ijheatmasstransfer.2019.118894>.
- [18] B. Samareh, O. Stier, V. Lüthen, A. Dolatabadi, Assessment of CFD modeling via flow visualization in cold spray process, *J. Therm. Spray Technol.* 18 (2009) 934–943, <https://doi.org/10.1007/s11666-009-9363-9>.
- [19] J. Pattison, S. Celotto, A. Khan, W. O'Neill, Standoff distance and bow shock phenomena in the cold spray process, *Surf. Coatings Technol.* 202 (2008) 1443–1454, <https://doi.org/10.1016/j.surcoat.2007.06.065>.
- [20] V.F. Kosarev, S.V. Klinkov, A.P. Alkhimov, A.N. Papyrin, On some aspects of gas dynamics of the cold spray process, *J. Therm. Spray Technol.* 12 (2003) 265–281, <https://doi.org/10.1361/105996303770348384>.
- [21] S. Yin, M. Zhang, Z. Guo, H. Liao, X. Wang, Numerical investigations on the effect of total pressure and nozzle divergent length on the flow character and particle impact velocity in cold spraying, *Surf. Coatings Technol.* 232 (2013) 290–297, <https://doi.org/10.1016/j.surcoat.2013.05.017>.
- [22] G. Huang, D. Gu, X. Li, L. Xing, H. Wang, Numerical simulation on siphonage effect of laval nozzle for low pressure cold spray system, *J. Mater. Process. Technol.* 214 (2014) 2497–2504, <https://doi.org/10.1016/j.jmatprotec.2014.05.014>.
- [23] A. Bacciochini, S. Bourdon-Lafleur, C. Poupart, M. Radulescu, B. Jodoin, Ni-Al nanoscale energetic materials: phenomena involved during the manufacturing of bulk samples by cold spray, *J. Therm. Spray Technol.* 23 (2014) 1142–1148, <https://doi.org/10.1007/s11666-014-0078-1>.
- [24] D. MacDonald, S. Leblanc-Robert, R. Fernández, A. Farjam, B. Jodoin, Effect of nozzle material on downstream lateral injection cold spray performance, *J. Therm. Spray Technol.* 25 (2016) 1149–1157, <https://doi.org/10.1007/s11666-016-0426-4>.
- [25] H. Che, X. Chu, P. Vo, S. Yue, Metallization of various polymers by cold spray, *J. Therm. Spray Technol.* 27 (2018) 169–178, <https://doi.org/10.1007/s11666-017-0663-1>.
- [26] D. MacDonald, R. Fernández, F. Delloro, B. Jodoin, Cold spraying of Armstrong process titanium powder for additive manufacturing, *J. Therm. Spray Technol.* 26 (2017) 598–609, <https://doi.org/10.1007/s11666-016-0489-2>.
- [27] S. Bagherifard, I. Fernández Pariente, R. Ghelichi, M. Guagliano, S. Vezzù, Effect of shot peening on residual stresses and surface work-hardening in cold sprayed coatings, *Key Eng. Mater.* 417–418 (2009) 397–400, <https://doi.org/10.4028/www.scientific.net/KEM.417-418.397>.
- [28] J.-O. Kliemann, H. Gutzmann, F. Gärtner, H. Hübler, C. Borchers, T. Klassen, Formation of cold-sprayed ceramic titanium dioxide layers on metal surfaces, *J. Therm. Spray Technol.* 20 (2011) 292–298, <https://doi.org/10.1007/s11666-010-9563-3>.
- [29] E. Sansoucy, P. Marcoux, L. Ajdelsztajn, B. Jodoin, Properties of SiC-reinforced aluminum alloy coatings produced by the cold gas dynamic spraying process, *Surf. Coatings Technol.* 202 (2008) 3988–3996, <https://doi.org/10.1016/J.SURFCOAT.2008.02.017>.
- [30] E. Sansoucy, G.E. Kim, A.L. Moran, B. Jodoin, Mechanical characteristics of Al-Ce coatings produced by the cold spray process, *J. Therm. Spray Technol.* 16 (2007) 651–660, <https://doi.org/10.1007/s11666-007-9099-3>.
- [31] W. Wong, A. Rezaeian, E. Irissou, J.G. Legoux, S. Yue, Cold spray characteristics of commercially pure Ti and Ti-6Al-4V, *Adv. Mater. Res.* 89–91 (2010) 639–644, <https://doi.org/10.4028/www.scientific.net/AMR.89-91.639>.
- [32] V.S. Bhattriprolu, K.W. Johnson, O.C. Ozdemir, G.A. Crawford, Influence of feedstock powder and cold spray processing parameters on microstructure and mechanical properties of Ti-6Al-4V cold spray depositions, *Surf. Coatings Technol.* 335 (2018) 1–12, <https://doi.org/10.1016/J.SURFCOAT.2017.12.014>.
- [33] D.L. Gilmore, R.C. Dykhuizen, R.A. Neiser, M.F. Smith, T.J. Roemer, Particle velocity and deposition efficiency in the cold spray process, *J. Therm. Spray Technol.* 8 (1999) 576–582, <https://doi.org/10.1361/105996399770350278>.
- [34] T.H.V. Steenkiste, J.R. Smith, R.E. Teets, Aluminum coatings via kinetic spray with relatively large powder particles, *Surf. Coatings Technol.* 154 (2002) 237–252, [https://doi.org/10.1016/S0257-8972\(02\)00018-X](https://doi.org/10.1016/S0257-8972(02)00018-X).
- [35] F. Raletz, M. Vardelle, G. Ezoo, Critical particle velocity under cold spray conditions, *Surf. Coatings Technol.* 201 (2006) 1942–1947, <https://doi.org/10.1016/j.surcoat.2006.04.061>.
- [36] X.-J. Ning, J.-H. Jang, H.-J. Kim, The effects of powder properties on in-flight particle velocity and deposition process during low pressure cold spray process, *Appl. Surf. Sci.* 253 (2007) 7449–7455, <https://doi.org/10.1016/J.APSUSC.2007.03.031>.
- [37] S. Yin, X. Wang, X. Suo, H. Liao, Z. Guo, W. Li, C. Coddet, Deposition behavior of thermally softened copper particles in cold spraying, *Acta Mater.* 61 (2013) 5105–5118, <https://doi.org/10.1016/j.actamat.2013.04.041>.
- [38] W.-Y. Li, H. Liao, G. Douchy, C. Coddet, Optimal design of a cold spray nozzle by numerical analysis of particle velocity and experimental validation with 316L stainless steel powder, *Mater. Des.* 28 (2007) 2129–2137, <https://doi.org/10.1016/J.MATDES.2006.05.016>.
- [39] Y. Xie, M.P. Planche, R. Raeelison, P. Hervé, X. Suo, P. He, H. Liao, Investigation on the influence of particle preheating temperature on bonding of cold-sprayed nickel coatings, *Surf. Coatings Technol.* 318 (2017) 99–105, <https://doi.org/10.1016/j.surcoat.2016.09.037>.
- [40] C.W. Zieman, W.J. Wright, D.E. Cipoletti, Influence of impact conditions on feedstock deposition behavior of cold-sprayed Fe-based metallic glass, *J. Therm. Spray Technol.* 27 (2018) 843–856, <https://doi.org/10.1007/s11666-018-0720-4>.
- [41] A. Sova, S. Grigoriev, A. Kochetkova, I. Smurov, Influence of powder injection point position on efficiency of powder preheating in cold spray: numerical study, *Surf. Coatings Technol.* 242 (2014) 226–231, <https://doi.org/10.1016/j.surcoat.2013.10.078>.
- [42] H.J. Kim, C.H. Lee, S.Y. Hwang, Fabrication of WC-Co coatings by cold spray deposition, *Surf. Coatings Technol.* 191 (2005) 335–340, <https://doi.org/10.1016/j.surcoat.2004.04.058>.
- [43] M.R. Rokni, S.R. Nutt, C.A. Widener, V.K. Champagne, R.H. Hrabe, Review of relationship between particle deformation, coating microstructure, and properties in high-pressure cold spray, *J. Therm. Spray Technol.* 26 (2017) 1308–1355, <https://doi.org/10.1007/s11666-017-0575-0>.
- [44] A. Nastic, M. Vijay, A. Tieu, S. Rahmati, B. Jodoin, Experimental and numerical study of the influence of substrate surface preparation on adhesion mechanisms of aluminum cold spray coatings on 300M steel substrates, *J. Therm. Spray Technol.* 26 (2017), <https://doi.org/10.1007/s11666-017-0602-1>.
- [45] A. Nastic, Repair of Aluminum Alloy Aerospace Components and Cold Gas Dynamic Spray Flow Distribution Study, University of Ottawa, 2015. <https://ruor.uottawa.ca/handle/10393/32998>.
- [46] A. International, Standard Test Method for Adhesion or Cohesion Strength of Thermal Spray Coatings, C633 - 13(2017), in: West Conshohocken, 2017.
- [47] ASTM D4145 - 10 (2018) standard test method for coating flexibility of prepainted sheet (n.d.). <https://www.astm.org/Standards/D4145.htm> (accessed September 2, 2020).
- [48] ANSYS FLUENT 12.0 theory guide - 15.2.2 turbulent dispersion of particles (n.d.). <https://www.ansys.com/project/neptunius/docs/fluent/html/th/node242.htm> (accessed April 3, 2020).
- [49] ANSYS FLUENT 12.0 theory guide - release 12.0, ANSYS-Guide. <https://www.ansys.com/project/neptunius/docs/fluent/html/th/node59.htm>, 2009. (Accessed 10 August 2020).
- [50] H. Tabbara, S. Gu, D.G. McCartney, T.S. Price, P.H. Shipway, Study on process optimization of cold gas spraying, *J. Therm. Spray Technol.* 20 (2011) 608–620, <https://doi.org/10.1007/s11666-010-9564-2>.
- [51] P. Liebersbach, A. Foelsche, V.K. Champagne, M. Siopis, A. Nardi, D.P. Schmidt, CFD simulations of feeder tube pressure oscillations and prediction of clogging in cold spray nozzles, *J. Therm. Spray Technol.* 29 (2020) 400–412, <https://doi.org/10.1007/s11666-020-00992-0>.
- [52] O.C. Ozdemir, C.A. Widener, Influence of powder injection parameters in high-pressure cold spray, *J. Therm. Spray Technol.* 26 (2017) 1411–1422, <https://doi.org/10.1007/s11666-017-0606-x>.
- [53] R. Lupoi, W. O'Neill, Powder stream characteristics in cold spray nozzles, *Surf. Coatings Technol.* 206 (2011) 1069–1076, <https://doi.org/10.1016/j.surcoat.2011.07.061>.
- [54] X. Suo, S. Yin, M.P. Planche, T. Liu, H. Liao, Strong effect of carrier gas species on particle velocity during cold spray processes, *Surf. Coatings Technol.* 268 (2015) 90–93, <https://doi.org/10.1016/j.surcoat.2014.04.039>.
- [55] C.B. Henderson, Drag coefficients of spheres in continuum and rarefied flows, *AIAA J.* 14 (1976) 707–708, <https://doi.org/10.2514/3.61409>.
- [56] B. Jodoin, F. Raletz, M. Vardelle, Cold spray modeling and validation using an optical diagnostic method, *Surf. Coatings Technol.* 200 (2006) 4424–4432, <https://doi.org/10.1016/j.surcoat.2005.02.209>.
- [57] T. Han, Z. Zhao, B.A. Gillispie, J.R. Smith, Effects of spray conditions on coating formation by the kinetic spray process, *J. Therm. Spray Technol.* 14 (2005) 373–383, <https://doi.org/10.1361/105996305X59369>.
- [58] V.K. Champagne, D.J. Helfritch, S.P.G. Dinavahi, P.F. Leyman, Theoretical and experimental particle velocity in cold spray, *J. Therm. Spray Technol.* 20 (2011) 425–431, <https://doi.org/10.1007/s11666-010-9530-z>.
- [59] S.V. Klinkov, V.F. Kosarev, A.A. Sova, I. Smurov, Calculation of particle parameters for cold spraying of metal-ceramic mixtures, *J. Therm. Spray Technol.* 18 (2009) 944–956, <https://doi.org/10.1007/s11666-009-9346-x>.
- [60] T. Saito, M. Saba, M. Sun, K. Takayama, The effect of an unsteady drag force on the structure of a non-equilibrium region behind a shock wave in a gas-particle mixture, *Shock Waves* 20 (2007) 255–262, <https://doi.org/10.1007/s00193-007-0109-7>.
- [61] A.M. Birt, V.K. Champagne, R.D. Sisson, D. Apelian, Microstructural analysis of Ti-6Al-4V powder for cold gas dynamic spray applications, *Adv. Powder Technol.* 26 (2015) 1335–1347, <https://doi.org/10.1016/J.APT.2015.07.008>.
- [62] T. Stoltenhoff, H. Kreye, H.J. Richter, An analysis of the cold spray process and its coatings, *J. Therm. Spray Technol.* 11 (2002) 542–550.
- [63] X.K. Suo, T.K. Liu, W.Y. Li, Q.L. Suo, M.P. Planche, H.L. Liao, Numerical study on the effect of nozzle dimension on particle distribution in cold spraying, *Surf. Coatings Technol.* 220 (2013) 107–111, <https://doi.org/10.1016/J.SURFCOAT.2012.09.029>.
- [64] C.Y. Wu, C. Thornton, L.Y. Li, Rebound behaviour of spheres during elastic-plastic oblique impacts, in: Int. World Scientific Publishing Company, *J. Mod. Phys. B*, 2008, pp. 1095–1102, <https://doi.org/10.1142/s0217979208046372>.

- [65] O.C. Ozdemir, Q. Chen, S. Muftu, V.K. Champagne, Modeling the continuous heat generation in the cold spray coating process, *J. Therm. Spray Technol.* 28 (2019) 108–123, <https://doi.org/10.1007/s11666-018-0794-z>.
- [66] J.C. Carling, B.L. Hunt, The near wall jet of a normally impinging, uniform, axisymmetric, supersonic jet, *J. Fluid Mech.* 66 (1974) 159–176, <https://doi.org/10.1017/S0022112074000127>.
- [67] A.G. McDonald, A.N. Ryabinin, E. Irisson, J.-G. Legoux, Gas-substrate heat exchange during cold-gas dynamic spraying, *J. Therm. Spray Technol.* 22 (2013) 391–397, <https://doi.org/10.1007/s11666-012-9828-0>.
- [68] R. Singh, K.H. Rauwald, E. Wessel, G. Mauer, S. Schruefer, A. Barth, S. Wilson, R. Vassen, Effect of substrate roughness and spray-angle on deposition behavior of cold-sprayed Inconel 718, *Surf. Coatings Technol.* 319 (2017) 249–259, <https://doi.org/10.1016/j.surfcoat.2017.03.072>.
- [69] P. Richer, B. Jodoin, L. Ajdelsztajn, E.J. Lavernia, Substrate roughness and thickness effects on cold spray nanocrystalline Al-Mg coatings, *J. Therm. Spray Technol.* 15 (2006) 246–254, <https://doi.org/10.1361/105996306X108174>.
- [70] S. Shin, S. Yoon, Y. Kim, C. Lee, Effect of particle parameters on the deposition characteristics of a hard/soft-particles composite in kinetic spraying, *Surf. Coatings Technol.* 201 (2006) 3457–3461, <https://doi.org/10.1016/j.surfcoat.2006.07.255>.
- [71] H. Assadi, F. Gärtner, T. Stoltenhoff, H. Kreye, Bonding mechanism in cold gas spraying, *Acta Mater.* 51 (2003) 4379–4394, [https://doi.org/10.1016/S1359-6454\(03\)00274-X](https://doi.org/10.1016/S1359-6454(03)00274-X).
- [72] K. Spencer, M.-X. Zhang, Optimisation of stainless steel cold spray coatings using mixed particle size distributions, *Surf. Coatings Technol.* 205 (2011) 5135–5140, <https://doi.org/10.1016/J.SURFCOAT.2011.05.020>.
- [73] J. Henao, A. Concstell, S. Dosta, N. Cinca, I.G. Cano, J.M. Guilemany, Influence of the substrate on the formation of metallic glass coatings by cold gas spraying, *J. Therm. Spray Technol.* 25 (2016) 992–1008, <https://doi.org/10.1007/s11666-016-0419-3>.
- [74] V.N. Zaikovskii, S.V. Klinkov, V.F. Kosarev, B.M. Melamed, G.V. Trubacheev, Control of spray spot shape in cold spray technology. Part 2. Spraying process, *Thermophys. Aeromechanics.* 21 (2014) 223–230, <https://doi.org/10.1134/S0869864314020085>.
- [75] H. Assadi, T. Schmidt, H. Richter, J.-O. Kliemann, K. Binder, F. Gärtner, T. Klassen, H. Kreye, On parameter selection in cold spraying, *J. Therm. Spray Technol.* 20 (2011) 1161–1176, <https://doi.org/10.1007/s11666-011-9662-9>.
- [76] J.G. Legoux, E. Irisson, C. Moreau, Effect of Substrate Temperature on the Formation Mechanism of Cold-sprayed Aluminum, Zinc and Tin Coatings. doi:<https://doi.org/10.1007/s11666-007-9091-y> (n.d.).
- [77] T. Schmidt, F. Gärtner, H. Assadi, H. Kreye, Development of a generalized parameter window for cold spray deposition, *Acta Mater.* 54 (2006) 729–742, <https://doi.org/10.1016/J.ACTAMAT.2005.10.005>.
- [78] A. Browning, C. Ortiz, M.C. Boyce, Mechanics of composite elasmoid fish scale assemblies and their bioinspired analogues, *J. Mech. Behav. Biomed. Mater.* 19 (2013) 75–86, <https://doi.org/10.1016/j.jmbbm.2012.11.003>.
- [79] R.G. Crookes, B. März, H. Wu, Ductile deformation in alumina ceramics under quasi-static to dynamic contact impact, *Mater. Des.* 187 (2020), 108360, <https://doi.org/10.1016/j.matdes.2019.108360>.